

Extreme emission-line galaxies out to $z \sim 1$ in zCOSMOS-20k

I. Sample and characterization of global properties

R. Amorín^{1,2}, E. Pérez-Montero^{2,3,4}, T. Contini^{3,4}, J.M. Vílchez², M. Bolzonella¹⁰, L. A. M. Tasca⁶, F. Lamareille^{3,4}, G. Zamorani¹⁰, C. Maier^{5,16}, C. M. Carollo⁵, J.-P. Kneib⁶, O. Le Fèvre⁶, S. Lilly⁵, V. Mainieri⁷, A. Renzini⁸, M. Scodeggio⁹, S. Bardelli¹⁰, A. Bongiorno¹¹, K. Caputi²¹, O. Cucciati¹³, S. de la Torre¹², L. de Ravel¹², P. Franzetti⁹, B. Garilli^{9,6}, A. Iovino¹⁴, P. Kampczyk⁵, C. Knobel⁵, K. Kovač^{5,15}, J.-F. Le Borgne^{3,4}, V. Le Brun⁶, M. Mignoli¹⁰, R. Pellò^{3,4}, Y. Peng⁵, V. Presotto^{17,14}, E. Ricciardelli¹⁸, J. D. Silverman¹⁹, M. Tanaka¹⁹, L. Tresse⁶, D. Vergani^{10,20}, and E. Zucca¹⁰

¹ INAF – Osservatorio Astronomico di Roma, via Frascati 33, 00040 Monteporzio Catone, Roma, Italy

² Instituto de Astrofísica de Andalucía, CSIC, 18008 Granada, Spain

³ IRAP, Université de Toulouse, UPS-OMP, Toulouse, France

⁴ Institut de Recherche en Astrophysique et Planétologie, CNRS, 14, avenue Edouard Belin, F-31400 Toulouse, France

⁵ Institute of Astronomy, ETH Zurich, CH-8093, Zürich, Switzerland

⁶ Laboratoire d'Astrophysique de Marseille, CNRS-Université d'Aix-Marseille, 38 rue Frederic Joliot Curie, F-13388 Marseille, France

⁷ European Southern Observatory, Karl-Schwarzschild-Strasse 2, Garching b. Muenchen, D-85748, Germany

⁸ Dipartimento di Astronomia, Università di Padova, vicolo Osservatorio 3, I-35122 Padova, Italy

⁹ INAF - IASF Milano, Via Bassini 15, I-20133, Milano, Italy

¹⁰ INAF - Osservatorio Astronomico di Bologna, via Ranzani 1, I-40127 Bologna, Italy

¹¹ Max-Planck-Institut für extraterrestrische Physik, D-84571 Garching b. Muenchen, D-85748, Germany

¹² SUPA Institute for Astronomy, The University of Edinburgh, Royal Observatory, Edinburgh, EH9 3HJ

¹³ INAF - Osservatorio Astronomico di Trieste, Via Tiepolo, 11, I-34143 Trieste, Italy

¹⁴ INAF - Osservatorio Astronomico di Brera, Via Brera, 28, I-20159 Milano, Italy

¹⁵ MPA - Max Planck Institut für Astrophysik, Karl-Schwarzschild-Str. 1, 85741 Garching, Germany

¹⁶ University of Vienna, Department of Astronomy, Tuerkenschanzstrasse 17, 1180 Vienna, Austria

¹⁷ Università degli Studi dell'Insubria, Via Valleggio 11, 22100 Como, Italy

¹⁸ Instituto de Astrofísica de Canarias, Vía Lactea s/n, E-38200 La Laguna, Tenerife, Spain

¹⁹ IPMU, Institute for the Physics and Mathematics of the Universe, 5-1-5 Kashiwanoha, Kashiwa, 277-8583, Japan

²⁰ INAF-IASFBO, Via P. Gobetti 101, I-40129, Bologna, Italy

²¹ Kapteyn Astronomical Institute, University of Groningen, 9700 AV Groningen, The Netherlands

ABSTRACT

Context. The characterisation of large and representative samples of low-metallicity star-forming galaxies at different cosmic epochs is of great interest to the detailed understanding of the assembly history and evolution of low-mass galaxies.

Aims. We present a large sample of 183 extreme emission-line galaxies (EELGs) at redshift $0.11 \leq z \leq 0.93$ selected from the 20k zCOSMOS Bright Survey by their unusually large $[\text{O III}] \lambda 5007$ equivalent widths. We characterise the EELGs on the basis of their main integral spectrophotometric properties, which are discussed along with their morphological and environmental properties.

Methods. Based on emission-line diagnostics, 165 purely star-forming EELGs and 18 narrow-line AGN candidates are identified. For star forming EELGs we use multiwavelength COSMOS photometry, HST-ACS *I*-band imaging and optical zCOSMOS spectroscopy to derive their main global properties, such as sizes, stellar masses, star formation rates (SFR) and reliable oxygen abundances using both “direct” and “strong-line” methods. Moreover, we propose a new method based on the use of the $[\text{O III}]$ electron temperature (the $t_e[\text{O III}]$ -Z calibration) to derive metallicities in EELGs without available $[\text{O II}]$ lines.

Results. EELGs are extremely compact ($r_{50} \sim 1.3$ kpc), low-mass ($M_\star \sim 10^7$ - $10^{10} M_\odot$) galaxies forming stars at unusually high rates (SFR up to $\sim 35 M_\odot \text{ yr}^{-1}$). They are among the highest specific SFRs (sSFR) galaxies in zCOSMOS, with stellar mass doubling times $0.01 \text{ Gyr} < M_\star / \text{SFR} < 1 \text{ Gyr}$. Consistently, the EELGs are luminous and extremely compact at rest-frame UV wavelengths ($L_{\text{FUV}} \sim 10^{10.4} L_\odot$ and $\mu_{\text{FUV}} \gtrsim 10^9 L_\odot \text{ kpc}^{-2}$, respectively) and include strong Ly α emitters, as revealed by GALEX spectroscopy. We show that zCOSMOS EELGs are low-metallicity systems, with $12 + \log(\text{O}/\text{H}) = 8.16 \pm 0.21$ ($0.2 Z_\odot$) in the median. Among them, we discover a handful of EELGs which are extremely metal-deficient ($< 0.1 Z_\odot$). Finally, HST-ACS *I*-band images reveal that $\sim 80\%$ of the EELGs show non-axisymmetric morphologies, including clumpy and cometary/tadpole galaxies, and a significant fraction ($\sim 29\%$) of galaxies with additional low surface brightness features strongly suggesting recent or ongoing interactions. As star-forming dwarfs in the local Universe, EELGs are preferably found in relative isolation. While only very few EELGs belong to compact groups, almost one third of them are found in spectroscopically confirmed loose pairs or triplets.

Conclusions. The zCOSMOS EELGs are galaxies caught in a transient and probably early period of their evolution, where they are efficiently building-up a significant fraction of their present-day stellar mass in an ongoing, galaxy-wide starburst. Therefore, the EELGs constitute an ideal benchmark for comparison studies between low- and high-redshift low-mass star-forming galaxies.

Key words. galaxies : evolution – galaxies : fundamental parameters – galaxies : abundances – galaxies : starbursts

1. Introduction

Low-mass galaxies undergoing vigorous bursts of star formation over galaxy-wide scales provide unique laboratories for understanding galaxy mass assembly and chemical evolution over cosmic times. These systems, often referred to as HII galaxies (Terlevich et al. 1991) and Blue Compact Dwarfs (BCDs Thuan & Martin 1981) in the local Universe – depending on the observational technique or selection criteria (see Kunth & Östlin 2000, for a review) – are generally recognized in spectroscopic surveys by their high excitation emission lines with unusually large equivalent widths, as a product of the photoionization of gas by hot massive stars from a young burst of star formation (Sargent & Searle 1970).

Over the last decade, the advent of all-sky optical and UV surveys such as the *Sloan Digital Sky Survey* (SDSS; Abazajian et al. 2003) and the *Galaxy Evolution Explorer* (GALEX; Martin et al. 2005), along with other smaller surveys, have allowed to systematically search and characterise relatively large samples of extreme emission-line galaxies (EELGs) out to the frontiers of the local Universe ($z \lesssim 0.3$, e.g. Kniazev et al. 2004; Kakazu et al. 2007; Overzier et al. 2008; Salzer et al. 2009; Cardamone et al. 2009; Cowie et al. 2010; Izotov et al. 2011; Shim & Chary 2013), making possible the discovery of an increasing number of extremely compact, low-metallicity galaxies with unusually high specific star formation rates (SFR, $s\text{SFR} = \text{SFR}/M_\star \sim 1\text{--}100 \text{ Gyr}^{-1}$) – such as e.g. the *green peas* (Cardamone et al. 2009; Amorín et al. 2010) – and a handful of extremely metal-deficient galaxies ($Z \lesssim 1/10 Z_\odot$) at $0.1 \lesssim z \lesssim 0.4$ (e.g. Kakazu et al. 2007; Hu et al. 2009; Cowie et al. 2010). Similarly to nearby HII galaxies and BCDs, these EELGs may constitute the youngest and chemically least evolved population of low- z star-forming galaxies (e.g. Searle & Sargent 1972; Rosa-González et al. 2007; Jaskot & Oey 2013), though some of them may also contain stellar populations older than ~ 1 Gyr (Papaderos et al. 2008; Amorín et al. 2012a). These properties make them unique probes to study the details of chemical enrichment, massive star formation and feedback processes in galaxies with physical properties, i.e. size, mass, SFR, metallicity, gas and dust relative content, most likely resembling those prevailing at high redshift, e.g., Lyman-break galaxies and Lyman- α emitters (e.g. Pettini et al. 2001; Finkelstein et al. 2011). Moreover, increasing observational evidence points to these young, low-metallicity star forming galaxies as the likely environments to host the progenitors of long duration GRBs (e.g. Christensen et al. 2004; Kewley et al. 2007; Savaglio et al. 2009; Guseva et al. 2011) and the most luminous supernovae (Chen et al. 2013; Lunnan et al. 2013).

In order to get a comprehensive understanding of the properties of EELGs as a class, to select best case studies for detailed analysis, and provide a valuable benchmark for comparative studies at higher redshifts, large and representative samples of EELGs must be assembled. Though EELGs are generally rare among local low-mass galaxies ($<0.5\%$ of galaxies in SDSS Kniazev et al. 2004), their frequency and significance in the context of the cosmic star formation rate density is expected to increase out to $z \sim 1$ (Guzman et al. 1997; Kakazu et al. 2007). However, due to their faintness and compactness, studying EELGs at these intermediate redshifts requires a great deal of observational effort. Thus, pioneering studies have been limited to relatively small samples of intrinsically luminous objects (e.g. Koo et al. 1995; Phillips et al. 1997).

In this context, recent deep multiwavelength surveys have offered a new avenue for studying chemical enrichment and starburst activity and its associated feedback processes in strongly star forming EELGs out to $z \sim 1$ and beyond (see e.g. Hoyos et al. 2005; van der Wel et al. 2011; Atek et al. 2011; Trump et al. 2011; Xia et al. 2012; Henry et al. 2013; Ly et al. 2014; Amorín et al. 2014a,b; Masters et al. 2014; Maseda et al. 2014). This is the case of the COSMOS survey (Scoville et al. 2007) and one of its spectroscopic follow-ups, the zCOSMOS-20k Bright Survey (Lilly et al. 2007). In particular, the wealth of high quality data – deep multiwavelength imaging and optical spectroscopy – provided by these surveys allow a thorough and systematic characterization of a large probe of faint ($I_{\text{AB}} \sim 22$ mag) EELGs out to $z \sim 1$, thus covering galaxies over a wide range of integral properties. While the large collection of deep broad- and narrow-band photometric measurements provided by COSMOS allow to derive luminosities and reliable stellar masses, HST-ACS I -band imaging provides the spatial resolution needed to study morphological properties. Moreover, zCOSMOS spectroscopy provides the required S/N to properly measure Balmer and forbidden emission lines which are needed to derive reliable measurements of ongoing SFR and metallicity. Remarkably, and despite their intrinsic difficulties, such as the measurement of temperature sensitive emission line ratios (e.g. [O III] 5007/4363), zCOSMOS spectroscopy allow to derive gas-phase metallicities through the so-called *direct* method (or T_e -method) for an unprecedented large number of EELGs at intermediate redshifts, including a number of strongly star-forming systems which are good candidates to be extremely metal-deficient ($\leq 1/10 Z_\odot$) galaxies.

In this paper, we present the first characterisation of the largest sample of galaxies with extreme nebular emission in the range $0.1 \lesssim z \lesssim 1$ assembled so far from the zCOSMOS-20k Bright Survey. Our main aim is to characterise their main key properties, namely size, stellar mass, metallicity and SFR, and discuss them as a function of morphology and environment. The characterization of this large sample of EELGs with properties derived using homogeneous criteria will be used in a companion paper (Amorín et al., in prep.; Paper II) to discuss possible evolutionary scenarios based on their position in different scaling relations involving mass, metallicity and SFR, among other observables. This will allow us to provide new observational constraints to the formation history of low-mass star-forming galaxies over cosmological timescales.

Our paper is organized as follows. In Section 2 we describe the parent sample, our data set, and the selection criteria adopted to compile the sample of EELGs. In Section 3 we present our results, including the adopted approach to derive the main physical properties of the sample, namely morphological and environmental properties, stellar masses, star formation rates and UV properties, as well as gas-phase metallicities. As part of this analysis, we also present an alternative method aimed at obtaining T_e -based metallicities in those EELGs without available measurements of the [O II] 3727,3729 doublet. Later, in Section 4 we highlight the discovery of a number of extremely metal-poor galaxy candidates, discuss the connection between EELGs and Ly α emitters and discuss the properties of EELGs as a function of morphology and large-scale environment. Finally, Section 5 summarises our main results.

Throughout this paper we adopt the standard Λ -CDM cosmology, i.e., $h = 0.7$, $\Omega_m = 0.3$ and $\Omega_\Lambda = 0.7$ (Spergel et al., 2007) and the magnitudes are given in the AB system.

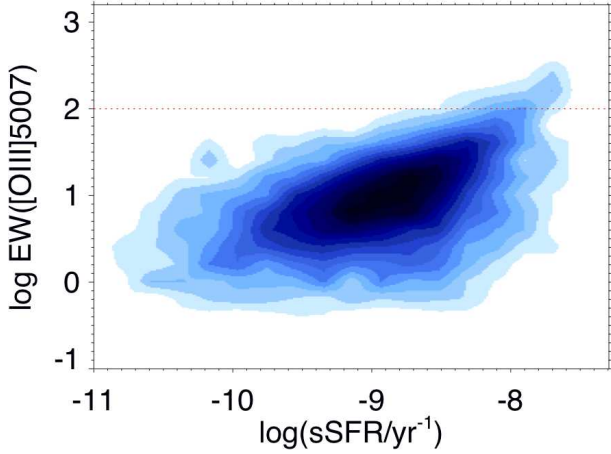


Fig. 1. [O III] λ 5007 equivalent width as a function of specific SFR for the SFG-20k sample by Pérez-Montero et al. (2013). The red dotted line delimits our selection threshold.

2. Sample and data

2.1. The parent zCOSMOS 20k-bright sample

The COSMOS survey is a large HST-ACS survey, with I -band exposures down to $I_{AB} = 28$ on a field of $\sim 2 \text{ deg}^2$ (Scoville et al. 2007). The COSMOS field has been the object of extensive multiwavelength ground- and space-based observations spanning the entire spectrum: X-ray, UV, optical/NIR, mid-infrared, mm/submillimeter and radio, providing fluxes measured over 30 photometric bands (Hasinger et al. 2007; Taniguchi et al. 2007; Capak et al. 2007; Lilly et al. 2007; Sanders et al. 2007; Bertoldi et al. 2007; Schinnerer et al. 2007; Koekemoer et al. 2007; McCracken et al. 2010).

The zCOSMOS survey (Lilly et al. 2007) is a large spectroscopic follow-up survey undertaken in the COSMOS field, which utilized about 600 h of ESO observing time with the VIMOS multi-object spectrograph (Le Fèvre et al. 2003) mounted on the Melipal 8m-telescope of the VLT. The zCOSMOS survey was divided in two parts, zCOSMOS-bright and zCOSMOS-deep. The zCOSMOS-deep observed $\sim 10\,000$ galaxies selected through color criteria to have $1.4 \lesssim z \lesssim 3.0$ on the central 1 deg^2 of the COSMOS field. The zCOSMOS-bright survey is purely magnitude-limited in I -band and covered the whole area of 1.7 deg^2 of the COSMOS field. The zCOSMOS-bright survey provides redshifts for $\sim 20\,000$ galaxies down to $I_{AB} \leq 22.5$ as measured from the HST-ACS imaging. The success rate in redshift measurements is very high, 95% in the redshift range $0.5 < z < 0.8$, and the velocity accuracy is $\sim 100 \text{ km/s}$ (Lilly et al. 2009). Each observed object has been assigned a flag according to the reliability of its measured redshift. Classes 3.x, 4.x redshifts, plus Classes 1.5, 2.4, 2.5, 9.3, and 9.5 are considered a secure set, with an overall reliability of 99% (see for details Lilly et al. 2009).

The current work is based on the zCOSMOS-bright survey final release, the so-called “20k-bright”. These consist of about 20 000 spectra for galaxies with $z \leq 2$ and secure redshifts according to the above flag classification (18 206 objects in total, irrespective of redshift and including stars). zCOSMOS-bright data were acquired with $1''$ -wide slits and the medium-resolution ($R = 600$) grism of VIMOS, providing spectra sampled at $\sim 2.5 \text{ Å pixel}^{-1}$ over a wavelength range of approximately $5550 - 9650 \text{ Å}$. This spectral range enables to follow important diagnostic emission lines to compute metallicity up to redshift

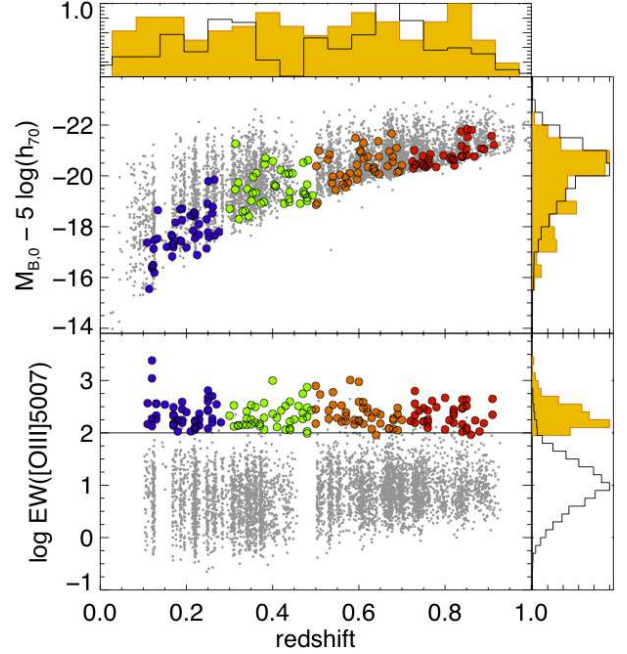


Fig. 2. Top panel shows the normalized redshift distribution of the SFG-20k sample (open) and the selected EELGs (filled). Middle and bottom panels show, respectively, the rest-frame B -band absolute magnitude and [O III] λ 5007 equivalent width of the selected EELGs (circles) and the SFGs-20K sample (dots) as a function of redshift. The colour code indicates bins of redshift: $0.11 \leq z \leq 0.30$ (purple), $0.30 < z \leq 0.50$ (green), $0.50 < z \leq 0.70$ (orange), and $0.70 < z \leq 0.93$ (red).

$z \sim 1.5$. The observations were acquired with a seeing lower than $1.2''$. The total integration time was set to 1 hour to secure redshifts with a high success rate. Detailed information about target selection, observations and data reduction can be found in Lilly et al. (2009).

Spectroscopic measurements (emission and absorption lines fluxes and equivalent widths) in zCOSMOS were performed through the automated pipeline *platefit-vimos* (Lamareille et al., in preparation) similar to that performed on SDSS (e.g. Tremonti et al. 2004) and VVDS spectra (Lamareille et al. 2009). This routine fits the stellar component of galaxy spectra as a combination of 30 single stellar population (SSPs) templates, with different ages and metallicities, from the library of Bruzual & Charlot (2003). The best-fit synthetic spectrum is used to remove the stellar component. Emission lines are then fitted altogether as a single nebular spectrum made of a sum of Gaussians at specified wavelengths. Further details can be found in Lamareille et al. (2006a, 2009).

2.2. The EELG sample selection

In Pérez-Montero et al. (2013) we selected a large subsample of more than 5300 star-forming galaxies at redshift $z = 0 - 1.3$ from the zCOSMOS-20k parent sample to study their physical properties and chemical evolution. In order to define our sample of EELGs, here we repeat the same procedure, discarding all broad-line AGNs and selecting only galaxies with $S/N > 2$ for all the emission-lines automatically measured by *platefit-vimos*, and involved in the derivation of the oxygen abundance. We limit the sample to ~ 5000 galaxies in the redshift range $0.11 \leq z \leq 0.93$ (hereafter referred to as the “SFG-20k sam-

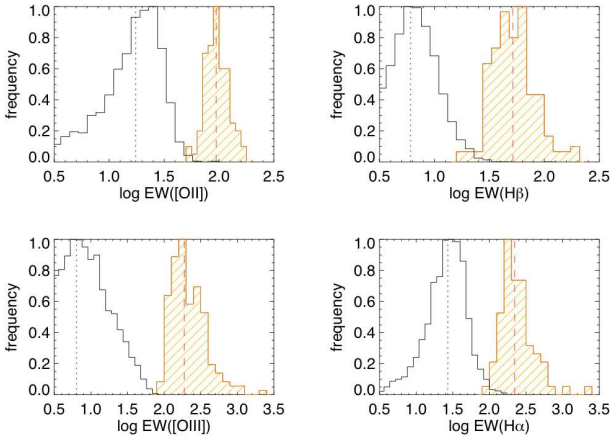


Fig. 3. Distribution of rest-frame equivalent widths for the most luminous hydrogen and oxygen emission lines of the SFG-20k (open) and EELG (lined) samples. The dashed and dotted lines indicate the median value in each case.

ple”) to keep only galaxies with $[\text{O III}] \lambda 5007$ still included in the observed spectral range. Finally, from the “SFG-20k sample” we select ~ 200 galaxies with the largest equivalent widths in $[\text{O III}]$, $\text{EW}([\text{O III}]) \geq 100 \text{ \AA}$, while the remaining galaxies in the SFG-20k sample are used as a comparison set.

The selection criteria for EELGs, based on the strength of $[\text{O III}] \lambda 5007$ emission line, is motivated by several reasons. Given the spectral range of VIMOS and the rest wavelength of $[\text{O III}]$, a selection criteria based on this line is more convenient compared to other strong lines (e.g. $\text{H}\alpha$ or $[\text{O II}]$) if one intends to maximize the redshift range to be explored. Thus, our selection criteria allow to collect EELGs from zCOSMOS-20k on a large redshift range, $0.11 \leq z \leq 0.93$. Moreover, as we show in Fig. 1, high $\text{EW}([\text{O III}])$ galaxies in the SFG-20k sample are those with largest *specific* SFRs. Despite the large scatter, the imposed limit in $\text{EW}([\text{O III}])$ for the EELGs guarantees that these systems are among the most efficient star-forming galaxies out to $z \sim 1$. Furthermore, the $[\text{O III}]$ criterion leads also to select galaxies with not only strong oxygen lines but also unusually strong hydrogen emission lines and extremely faint and flat continuum, as evidenced by the extremely large equivalent widths of $\text{H}\alpha$, $\text{H}\beta$, or $[\text{O II}]$, as we show in Fig. 3. Comparing $[\text{O III}]$ and $\text{H}\alpha$ equivalent widths, we show in Fig. 3 that our criterion based on $\text{EW}([\text{O III}])$ leads also to select galaxies with very high $\text{EW}(\text{H}\alpha) \geq 100 \text{ \AA}$ and $\text{EW}(\text{H}\beta) \geq 20 \text{ \AA}$. In contrast, an alternative selection criteria based on other strong emission line would have the drawback that we could only select a smaller number of galaxies over a smaller redshift range, e.g. $z \lesssim 0.5$ for $\text{H}\alpha$. Finally, the choice of a sample based on $[\text{O III}] \lambda 5007$, has been also motivated by the aim of collecting a representative and statistically significant sample of star-forming galaxies that would be easily detectable at high redshifts ($z \sim 2-3$) in deep wide-field NIR surveys (e.g. van der Wel et al. 2011; Atek et al. 2011; Xia et al. 2012; Guaita et al. 2013; Maseda et al. 2013, 2014). Since they would be affected by similar biases, our sample is intended to offer a valuable benchmark for future direct comparison with other probes of strong emission-line galaxies at higher redshifts.

Most of the selected galaxies are faint, with observed I_{AB} magnitudes of about ~ 22 mag. This can make the measurement of their continuum and faint emission-lines relatively uncertain when done with automatic procedures. In order to double check the equivalent widths and fluxes in our EELG sample we have re-

measured by hand (using the *splot* task in IRAF) all their emission lines to be sure of their values. Uncertainties for the line fluxes have been computed following Pérez-Montero & Díaz (2003). After discarding few spurious cases (i.e. extremely noisy spectra or with some defect) we finally define a total sample of 183 EELGs, which are uniformly distributed in redshift out to $z \sim 1$, as shown in Fig. 2. The EELGs are systematically found among the lower luminosity star-forming galaxies in zCOSMOS-20k. Their rest-frame broad-band luminosities increase with redshift, following the trend of the SFG-20k sample. Thus, EELGs occupy a broad luminosity range, with rest-frame B-band absolute magnitudes $-16 \lesssim M_B \lesssim -21.5$, including galaxies that can be considered as genuine *dwarfish* systems.

2.3. Identification of AGNs: diagnostic diagrams

In order to distinguish between purely and non-purely star-forming galaxies in the EELGs sample, we just need to identify narrow-line (NL) AGNs (Seyfert 2 and LINERs) because broad-line AGNs were previously excluded from the sample in the selection process. To do that, we use the combination of three empirical diagnostic diagrams based on different bright emission-line ratios, depending on their availability due to the galaxies’ redshift range. These diagrams are presented in Fig. 4. Moreover, we cross-correlate our sample galaxies with the XMM and Chandra X-rays catalogues from COSMOS (Hasinger et al. 2007; Elvis et al. 2009).

For galaxies at $z < 0.46$, and depending on the set of lines with reliable measurements available, we use both the well-known and commonly used diagnostic diagram (e.g. Baldwin et al. 1981; Veilleux & Osterbrock 1987) based on the line ratios $[\text{O III}]/\text{H}\beta$ and $[\text{N II}]/\text{H}\alpha$ (Fig. 4a), and the $\text{H}\alpha$ classification proposed by Lamareille et al. (2007) based on $[\text{N II}]$, $[\text{S II}]$, and $\text{H}\alpha$ emission-line ratios (Fig. 4b). Galaxies with line ratios above the limits imposed by these diagnostics are considered AGN candidates. For galaxies with $z > 0.46$, the $\text{H}\alpha$, $[\text{N II}] \lambda 6584$, and $[\text{S II}] \lambda \lambda 6717, 6731$ emission lines are not visible anymore in the observed wavelength range of zCOSMOS spectra and therefore the above diagnostics cannot be used. Instead, we use here the diagnostic diagram defined by Lamareille et al. (2004), involving the $[\text{O III}]/\text{H}\beta$ and $[\text{O II}]/\text{H}\beta$ emission-line ratios, and the corrections proposed by Pérez-Montero et al. (2013) to minimize the impact of reddening effects due to the long wavelength baseline between $[\text{O II}] \lambda 3727$ and $\text{H}\beta$ (Figure 4c). Galaxies above the curve defined by Marocco et al. (2011) are considered in this diagram as AGN candidates. While all these empirical limits have an uncertainty of about 0.2 dex, most EELGs in these diagrams are located close or within them when taking into account their error bars. Thus, we have checked one-by-one for the presence of bright high-ionization emission lines (e.g. $[\text{Ne V}]$) or very extended Balmer line components, which can be indicative of the presence of AGNs.

Overall, the agreement between the three different diagnostics is broadly good. Similar findings, although with slightly larger dispersion, are found using alternative diagnostics, such as the diagrams defined by excitation and stellar mass (Juneau et al. 2011) or excitation and $U-B$ colour (Yan et al. 2011). Only four EELGs, all of them at $z > 0.46$, are confirmed X-ray sources (zCOSMOS IDs 819469, 825103, 839230 and 841281). All of them are also clear AGN candidates in the optical diagnostics. While these are indicated as black open squares in Fig. 4, those AGN candidates without X-ray counterpart are indicated by triangles. All these AGN candidates show high ionization lines

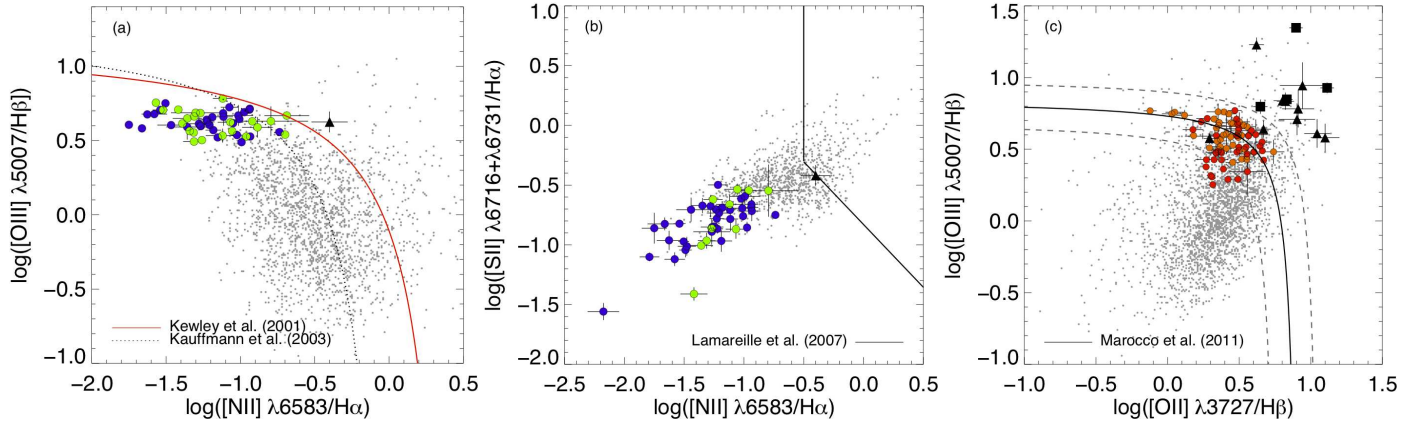


Fig. 4. Diagnostic diagrams. Purely star-forming systems and AGN candidates are indicated by colour and black symbols, respectively. The colour code indicates different redshift bins, as in Fig. 2. In panel *c* the AGN candidates with and without X-ray counterparts are indicated by squares and triangles, respectively.

such as [N_{II}] and H_{II} and have redder colours and stellar masses significantly higher than the rest of the EELGs. While AGN candidates are typically larger in size than purely star-forming EELGs, as we show below, they tend to show nearly round shapes with a central high surface brightness component rather than highly disturbed, irregular or clumpy morphologies.

In all, using the above criteria, our analysis yields 165 purely star-forming EELGs (90%) and 18 EELGs (10%) with likely NL-AGN contribution. In Fig. 5 we present one example of VIMOS spectrum for both a purely star-forming EELG and a NL-AGN candidate with X-ray counterpart.

3. The properties of extreme emission-line galaxies in zCOSMOS 20k

In this section we present the methods applied to derive the main global properties of star-forming EELGs and discuss briefly our results. In Table 1 we list a number of these properties for each galaxy¹. In order to further examine possible trends on their main properties with redshift, we split our sample of EELGs in four redshift bins. These redshift bins are almost equally populated and are shown with different colour codes in our figures. Table 2 shows median values and standard deviations of the main properties of EELGs according to these redshift bins, their optical morphology – as defined by the classification presented below – and according to their environmental properties. The median properties of the NL-AGN candidates, which are not considered for the subsequent analysis, are also included in Table 2.

3.1. The diverse morphologies of EELGs

Our first approach to study the morphological properties of the EELG sample comes from a visual classification using the HST/ACS *F814W*-band images. We exclude from the analysis the only five EELGs in the sample that have not been imaged by the ACS and are nearly unresolved in ground-based images. Inspired in classical visual classifications of BCDs (e.g. Cairós et al. 2001) we distinguish here four major morphological classes of EELGs according to the distribution and shape of their high and low surface brightness components:

1. *Round/Nucleated*, containing galaxies showing one bright resolved star-forming knot embedded in a nearly symmetric low surface brightness envelope and galaxies with point-like/unresolved appearance. About 18% of EELGs lie in this class.
2. *Clumpy/Chain*, containing galaxies with two or more high surface brightness knots spread out over a diffuse or asymmetric low surface brightness component. These EELGs represent ~ 37% of the sample galaxies.
3. *Cometary/Tadpole*, or galaxies with one or more bright star-forming knots located towards the tip of an extended, low surface brightness component. About 16% of the EELGs lie in this class.
4. *Merger/Interacting*, or galaxies with a distorted low surface brightness component, features clearly identified with signs of past or current interaction with very close companions, e.g. tails, bridges, etc. These EELGs are about the 29% of the sample.

Morphological classes for the sample of EELGs are given in Table 1, while several illustrative examples are shown in Fig. 6. None of the above classes appear to be biased to any redshift bin, showing all of them nearly the same median redshift. It is worth mentioning that EELGs belonging to the last three classes can be simply considered as “irregular” galaxies. Although there might be an inevitable overlap between them – e.g. some clumpy/chain or cometary/tadpole EELGs may be also interpreted in terms of interactions – a more detailed description of both the distribution of the star-forming regions and the shape of the underlying diffuse component in broad-band images remains interesting. In particular, it may be useful to study the possible mechanisms responsible for the origin of the starburst and chemical enrichment in these galaxies (e.g. Papaderos et al. 2008; Filho et al. 2013; Sánchez Almeida et al. 2013, 2014) and for comparing with galaxies of similar morphologies identified at higher redshifts (e.g. Elmegreen et al. 2012, 2013).

In addition to our visual classification, we quantify the morphological properties of EELGs using different parameters from the zCOSMOS 10k catalogue by Tasca et al. (2009). Since this catalogue includes ~ 70% of the EELG sample we derive here the morphological parameters for the remaining EELGs of the sample following the same method used by Tasca et al. (2009). In short, we use high-resolution imaging in the *F814W* filter from the HST/ACS to perform quantitative morphology using an optimised automated method to provide standard morpho-

¹ A preview table is shown. A complete version of this table is available *on-line*

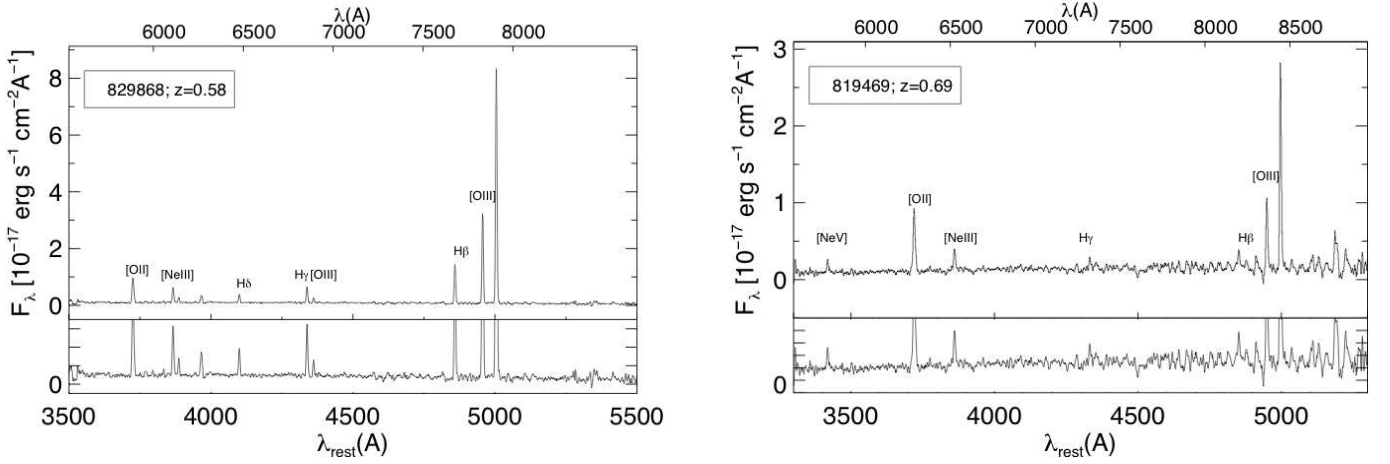


Fig. 5. VIMOS observed spectrum of the purely star-forming EELG 829868 at $z = 0.58$ (Left) and the NL-AGN candidate EELG 819469 at $z = 0.69$ (Right). The spectra have been smoothed by a 2 pixels filter. Lower and upper x -axis show rest-frame and observed wavelengths, respectively. The main emission lines detected are indicated in each case.

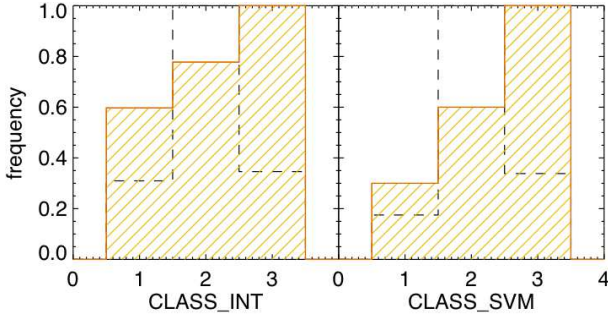


Fig. 7. (a): Normalized distribution of morphological classes: 1 = *elliptical*, 2 = *spiral*, and 3 = *irregular*, for EELG (lined) and normal SFGs in zCOSMOS (open) according to the classification schemes by Tasca et al. (2009) (left) and Huertas-Company et al. (2008) (right)

logical parameters, such as half-light radius, R_{50} and axial ratio, $q = b/a$, concentration index (C), asymmetry (A), and Gini coefficient (G), and classify the galaxies in three morphological classes, i.e. *early*, *spiral*, and *irregular*, according to different classification schemes (e.g. Abraham et al. 1996; Huertas-Company et al. 2008; Tasca et al. 2009). We show in Fig. 7 the normalized distributions of SFGs and EELGs over the three morphological classes and according to different classification schemes. Based on independent methods, these schemes are in good agreement. Most SFGs and EELGs show irregular shape and, therefore, they are automatically classified as *spiral* and *irregular*. However, the EELGs contain significantly higher fraction of galaxies automatically classified as *irregular* compared with the normal SFGs in zCOSMOS.

We find an agreement between the results of the classification schemes shown in Fig. 7 and our visual classification, in the sense that almost all the EELGs with “cometary/tadpole”, “clumpy/chain” and “merger/interacting” classification are automatically classified as “irregular” or “spiral”, whereas most EELGs classified as “round/nucleated” are classified as “elliptical”. Taken together, we conclude that at least $\sim 80\%$ of the sample present non-axisymmetric morphologies.

In Figure 8 we show the normalised distribution of morphological parameters for the two samples. The EELGs are small

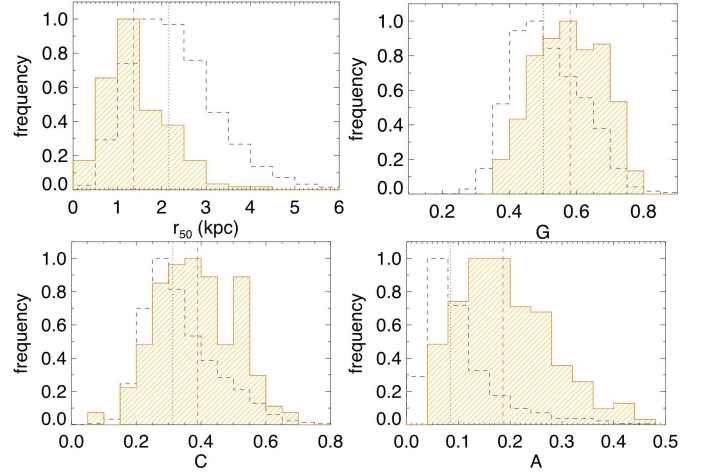


Fig. 8. Normalized distribution of morphological parameters, i.e. effective radius (a), Gini coefficient (b), concentration index (c), and asymmetry coefficient (d) for the 20k-SFG sample (open) and the sample of EELGs (lined). Dotted and continuous vertical lines indicate their corresponding median values.

systems, with half-light radii² spreading in a narrow range with median value of about 1.3 kpc. Similarly to most galaxies in the 20k-SFG sample, the C , A , and G parameters for the EELGs spread over a large range of values. However, there is a clear tendency in the EELGs to show larger asymmetry and also higher concentration and Gini parameters than normal SFGs. This result is also shown in Fig. 9 where we present the asymmetry-concentration and asymmetry-Gini diagrams for both zCOSMOS SFGs and EELGs. Especially at lower concentrations, the EELGs show larger asymmetry than normal SFGs at a given C or G . From Fig. 9 we can also test the consistency between both visual and quantitative classifications. Those EELGs visually classified as “round/nucleated” show higher concentration and Gini parameters than those included in “irregular” classes. From Fig. 9 is also noticeable the difficulty of distinguishing between galaxies with different “irregular” morphologies, such as

² We have circularized the half-light radii as $r_{50} = R_{50} q^{0.5}$, where q is the axial ratio, b/a . Both quantities have been measured from the I -band ($F814W$) HST-ACS images.

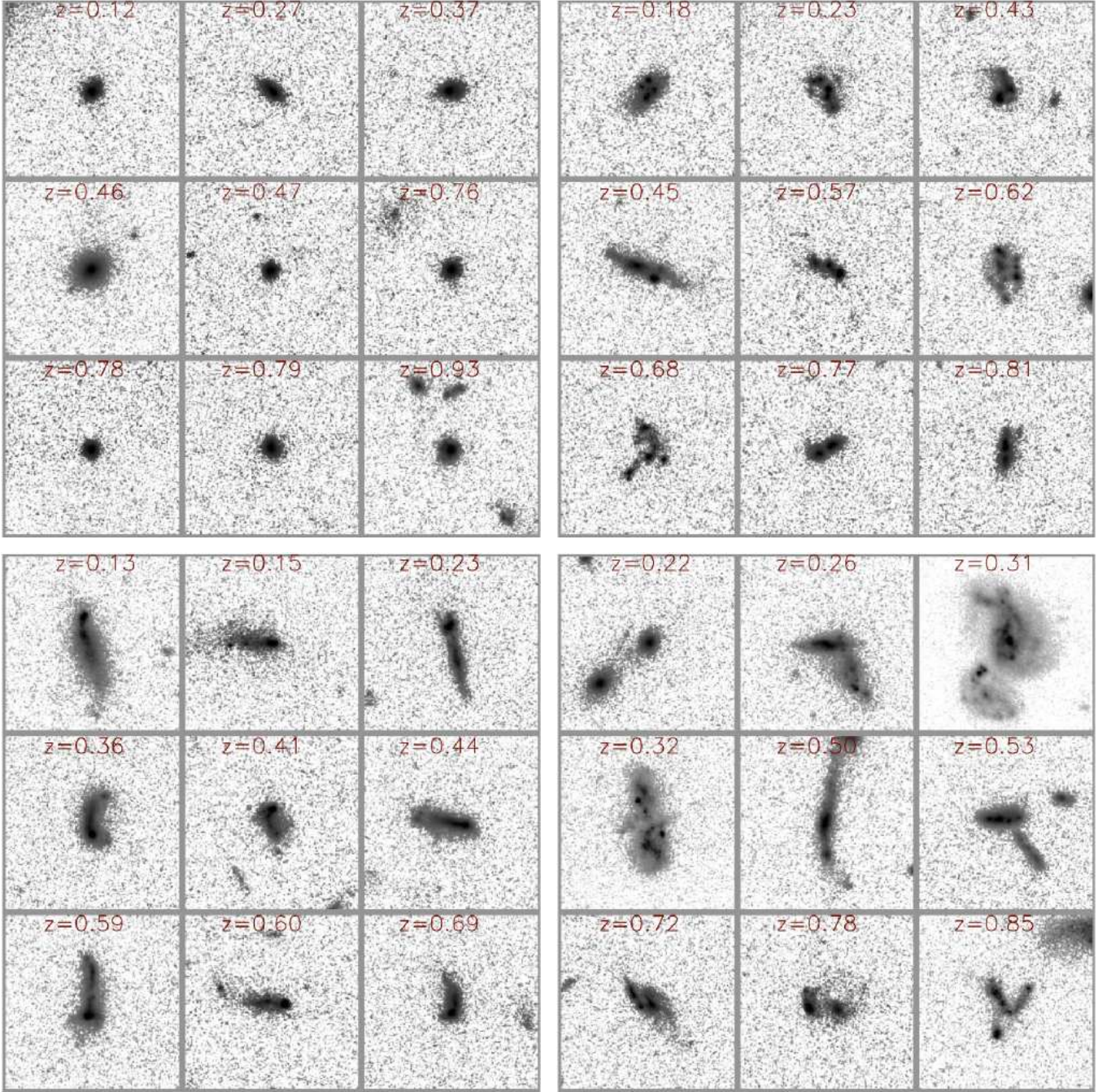


Fig. 6. The morphology of star-forming EELGs. Examples of “Round/Nucleated” (Upper-left), “Clumpy/Chain” (Upper-right), “Cometary/Tadpole” (Bottom-left), and “Merger/Interacting” (Bottom-right) morphologies from their HST/ACS *I*-band (*F814W*) images. North-East oriented images are 6'' on a side. The redshift for each galaxy is indicated in labels.

“cometary” or “clumpy” galaxies on the basis of such quantitative diagrams only.

3.2. The local environment of EELGs

We study the large scale environment of the EELG sample using the zCOSMOS-20k Group Catalogue (Knobel et al. 2012). This optical catalogue includes about 16500 galaxies between $0.1 \lesssim z \lesssim 1$, and contains 1498 groups in total, with 192 of them with more than five members. Full details about the catalogue can be found in Knobel et al. (2009, 2012). A cross-match between the group catalogue and our parent SFG-20k sample show

~ 26% of these galaxies in groups of 2 (16%) or more spectroscopic members. Similarly, the cross-match between the group catalogue and our 165 purely star-forming EELGs yields a total of 47 EELGs (~ 29%) catalogued as members of a group (i.e. with a probability $\geq 50\%$ and $\geq 90\%$ in 46 and 34 of them, respectively). Out of these 47 galaxies, 26 EELGs belong to pairs of galaxies, 11 belong to triplets, and only 10 of them belong to groups of four or more spectroscopic members. The probability that these EELGs are the most massive galaxy of their group is $\leq 10\%$ for all but five EELGs, all of them in pairs. Only two galaxies in our sample, zCOSMOS 823693 and zCOSMOS 823694, constitute by their own a spectroscopic pair of

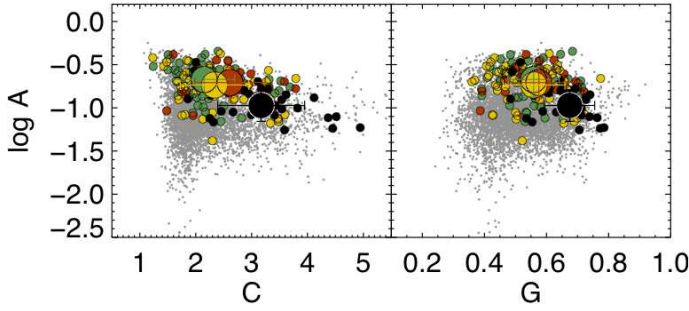


Fig. 9. Asymmetry-concentration (*Left*) and asymmetry-Gini (*Left*) diagrams for zCOSMOS SFGs (grey dots) and EELGs (colour circles). Yellow, red, green and black colours indicate EELGs visually classified as “merger/interaction”, “cometary/tadpole”, “clumpy/chain” and “round/nucleated”, respectively. The latter category can be distinguished from the other EELGs morphological classes in these morphological diagrams, as shown by their median values (large colour circles).

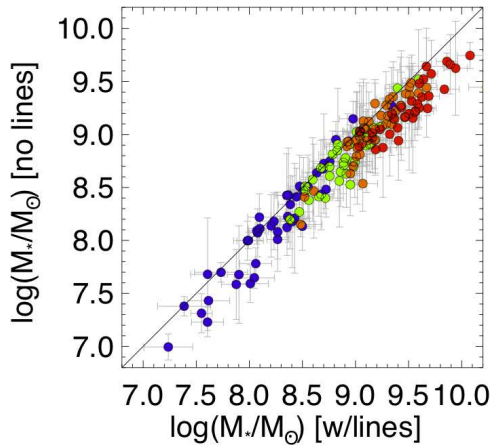


Fig. 10. Comparison of stellar masses derived from SED fitting before (*y*-axis) and after (*x*-axis) removing the contribution of emission lines fluxes to the broad-band photometry.

EELGs. The median properties of EELGs in groups are shown in Table 2.

Although EELGs do not show a preference for lower-density regions compared with the parent SFG-20k sample, we conclude that they tend to be in relative isolation, with $\sim 30\%$ of them with at least one spectroscopically confirmed companion, in good agreement with previous findings for local star-forming dwarf galaxies (e.g. Vílchez 1995; Lee et al. 2000; Noeske et al. 2001; Pustilnik et al. 2001; Cardamone et al. 2009). However, it is worth mentioning that most of the identified pairs and triplets are found to contain a larger number of photometric members, which may constitute in most cases neighbours of lower luminosity, as we discuss in Section 4.

3.3. The stellar masses of EELGs

Total stellar masses, M_* , for galaxies in the zCOSMOS parent sample are taken from Bolzonella et al. (2010). They were derived by fitting stellar population synthesis models to both the broad-band optical/near-infrared (CFHT: u , i , K_s ; Subaru: B , V , g , r , i , z Capak et al. 2007) and infrared (Spitzer/IRAC: $3.6\mu\text{m}$, $4.5\mu\text{m}$ Sanders et al. 2007) photometry using a chi-square minimization for each galaxy. The different methods used to compute

stellar masses, based on different assumptions about the population synthesis models and the star formation histories, are described in detail in Bolzonella et al. (2010). The accuracy of the photometric stellar masses is satisfactory overall, with typical dispersions due to statistical uncertainties and degeneracies of the order of 0.2 dex. The addition of secondary bursts to a continuous star formation history produces systematically higher (up to 40%) stellar masses, while population synthesis models taking into account the TP-AGB stellar phase (Maraston 2005) produces systematically lower M_* by 0.10 dex. The uncertainty on the absolute value of M_* due to assumptions on the Initial Mass Function (IMF) is within a factor of 2 for the typical IMFs usually adopted in the literature. In this paper, we have adopted stellar masses calculated on the basis of a Chabrier (2003) IMF and the stellar population models of Bruzual & Charlot (2003), with the addition of secondary bursts to the standard declining exponential star formation history.

For strong emission line galaxies a significant contribution to the broad-band flux densities from nebular emission is superposed to the stellar spectral energy distribution (SED). Since standard stellar population synthesis models do not include nebular emission this may have an impact on the SED fitting and, in particular, on the computed total stellar masses (e.g. Krueger et al. 1995; Papaderos et al. 1998; Schaerer & de Barros 2009; Atek et al. 2011; Curtis-Lake et al. 2013; Stark et al. 2013; Castellano et al. 2014). In order to overcome this potential systematic effect for the sample of EELGs, an additional set of fits were computed after removing the contribution of emission line fluxes to the observed broad-band magnitudes. For the models we follow the prescriptions described above for the standard zCOSMOS SED fitting (Bolzonella et al. 2010), but fixing the available stellar metallicity of stellar population models (from $Z = [0.02, 0.2, 0.4, 1] Z_\odot$) to the nearest value to the observed gas-phase metallicity of each galaxy (see Section 3.6). In those cases where the gas-phase metallicity was not available the median metallicity for the whole sample was adopted as a reference value.

We find that the stellar masses derived from the two prescriptions are mutually consistent. However, stellar masses derived from SED fitting using uncorrected magnitudes and solar metallicities are systematically offset to higher values (~ 0.25 dex in the median), as shown in Fig. 10. In the most extreme cases for our sample neglecting nebular emission in SED fitting may lead to an overestimation of the stellar mass of up to a factor of ~ 3 -5. This result is in good agreement with previous findings for strong emission line galaxies at low and high redshift (e.g. Atek et al. 2011; Curtis-Lake et al. 2013). In Table 1 we include the stellar masses for each EELG, while the median values for each redshift bin are listed in Table 2. In Figure 11b we show the distribution of M_* with redshift as compared with those of the 20k-SFG sample. EELGs are clearly among the lower-mass systems found by zCOSMOS. Stellar masses go from $\sim 10^7$ to $\sim 10^{10} M_\odot$, with a clear positive trend with redshift. In Figure 11b we show the limiting mass for the entire 20k-SFG sample as derived by Pérez-Montero et al. (2013). Most of the EELGs are between the 25% and 75% completeness limit (solid and dotted lines, respectively). Therefore, the EELGs are found to be in a range of masses where the zCOSMOS 20k sample is not complete.

3.4. Dust extinction and star formation rate of EELGs

We derive SFRs using the luminosity of the brightest available Balmer emission line after correction for aperture effects and

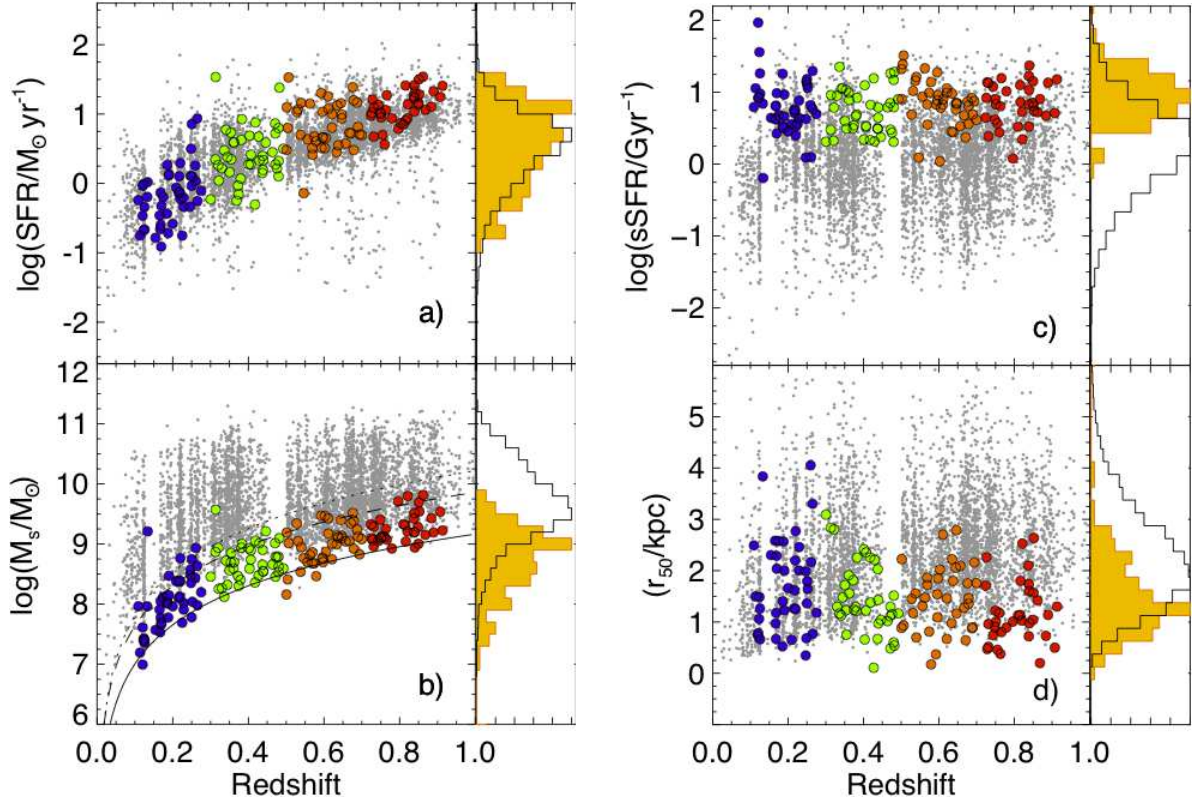


Fig. 11. Redshift distributions of SFR (a), stellar mass (b), specific SFR (c) and half-light radii (d). Solid, dashed and dotted lines in panel b show the logarithmic fitting to the limiting masses of the star-forming sample for levels 25%, 50%, and 75% of completeness, respectively. Symbols and colours are the same as in Fig. 2.

reddening. Aperture effects were quantified using factors derived from photometry³. Reddening correction was carried out using the Balmer decrement for those objects with more than one Balmer hydrogen recombination line with $S/N > 2$ available, and assuming the theoretical ratios at standard conditions of temperature and density from Storey & Hummer (1995) and the Cardelli et al. (1989) extinction law. Although gas extinction is preferable to be used whenever possible, for a number of galaxies where only one Balmer line is available ($\sim 9\%$ of the EELGs and $\sim 36\%$ of the SFG-20k sample), we considered a reddening coefficient from the stellar $E(B - V)$ parameter derived from the stellar synthesis fitting, assuming that the gas and the stellar reddening coefficients are correlated (Calzetti et al. 2000). The same rule was applied for $\sim 32\%$ of the EELGs where the line ratios $H\alpha/H\beta$ or $H\beta/H\gamma$ were lower than their theoretical values, i.e. $(H\alpha/H\beta)_0 = 2.82$ and $(H\gamma/H\beta)_0 = 0.47$, assuming Case B recombination for typical values of both electron temperature and density, $T_e = 2 \times 10^4 \text{ K}$ and $n_e = 100 \text{ cm}^{-3}$. The reddening distribution for the sample of EELGs is presented in Fig. 13(right). All galaxies show relatively low dust extinction, with a median value of $E(B - V) = 0.19$ magnitudes.

We derive the *ongoing* star formation rates from extinction-corrected $H\alpha$ luminosities and using the standard calibration by Kennicutt (1998), $\text{SFR}(H\alpha) = 7.9 \times 10^{-42} L(H\alpha) [\text{erg s}^{-1}]$, which assumes a Salpeter IMF from 0.1 to $100 M_\odot$. We have scaled down these SFRs by a factor of 1.7 to be consistent with the Chabrier IMF used along this paper. For those galaxies at $z > 0.44$ for which $H\alpha$ is not observed in the VIMOS spectra, we derive the expected $H\alpha$ luminosity based on the $H\beta$ fluxes and

the theoretical coefficients between Balmer hydrogen lines from Storey & Hummer (1995) for $T_e = 2 \times 10^4 \text{ K}$ and $n_e = 100 \text{ cm}^{-3}$.

We find that EELGs span a large range of $\text{SFR} \sim 0.1\text{--}35 M_\odot \text{ yr}^{-1}$, with median values increasing with redshift, as shown in Fig. 11a and in Table 2. These high SFRs in combination with their low stellar masses imply that EELGs include the most efficient star-forming galaxies of zCOSMOS 20k in terms of *specific* SFR, which is nearly constant with redshift and shows a median value of $\log(\text{sSFR}) \sim 0.81 \text{ Gyr}^{-1}$, as shown in Fig. 11c. The extremely high sSFRs of EELGs imply that they are rapidly building up their stellar components. Their stellar mass *doubling* times (i.e. $1/\text{sSFR}$, or the time needed to double their total stellar mass at their current SFR) are typically of a few hundreds million years.

3.4.1. UV properties

Galaxy Evolution Explorer (GALEX) data in the FUV ($\lambda_c \sim 1530 \text{ \AA}$) and NUV ($\lambda_c \sim 2315 \text{ \AA}$) from the COSMOS/GALEX photometric catalogue (Schiminovich et al. 2007; Zamojski et al. 2007) were used to derive rest-frame UV luminosities and colours for most of the EELGs. We calculate rest-frame FUV absolute magnitudes consistently with those in the optical and IR used for the SED fitting and stellar mass derivation (Bolzonella et al. 2010). In order to account for intrinsic dust attenuation, we have adopted the relation between the total dust attenuation and UV spectral slope given by Meurer et al. (1999) for a sample of local starbursts with IR and UV measurements, which can be expressed as $A_{\text{FUV}} = 4.43 + 1.99 \beta_{\text{UV}}$. In this equation

³ ACS-HST photometry was used if available, Subaru photometry if not

$\beta_{UV} = 2.32(FUV - NUV) - 2.0$ is the photometric measure of the UV spectral slope in rest-frame.

The resulting dust-corrected FUV luminosities, L_{FUV} , for each galaxy are listed in Table 1. Median values of β_{UV} and L_{FUV} are also included in Table 2. Our EELG sample shows typical values of $\beta_{UV} = -1.61$, which according to the Meurer’s formula imply dust attenuations of $A_{FUV} \sim 1.23$ mag. This value is $\sim 30\%$ lower than the one derived from a mean reddening derived from the optical of $E(B - V) \sim 0.2$ assuming a Cardelli et al. (1989) extinction law with $A_{FUV} = 8.15 E(B - V)$. After dust corrections we find for EELGs median luminosities of $L_{FUV} \sim 10^{10.4} L_{\odot}$ and FUV surface brightnesses⁴ of $\mu_{FUV} \gtrsim 10^9 L_{\odot} \text{ kpc}^{-2}$. These values provide a confirmation that the EELGs are very compact and luminous in the UV continuum. Compared with other samples of strong emission line galaxies the UV properties of the zCOSMOS EELGs are very similar to some local ($z \lesssim 0.3$) super compact UV-luminous galaxies discovered in *GALEX* surveys (e.g. Overzier et al. 2008; Hayes et al. 2013).

Using the dust-corrected FUV luminosities we also derive FUV-based SFRs using the calibration given by Kennicutt (1998), $SFR_{FUV} = 1.4 \times 10^{-28} L_{FUV} [\text{erg s}^{-1} \text{ Hz}^{-1}]$, scaled down to a Chabrier IMF. Even though the scatter is relatively large, both $SFR_{H\alpha}$ and SFR_{FUV} are in excellent agreement, as shown in Fig. 12. Since SFR_{FUV} traces massive star formation over a longer timescale than $H\alpha$ (typically up to a factor of 10 Kennicutt & Evans 2012), this would imply that these galaxies are experiencing a very recent and probably the first major star formation episode over the last several hundreds years. We note, however, that compared with the SFR derived from the SED fitting both $SFR_{H\alpha}$ and SFR_{FUV} are systematically lower by ~ 0.2 dex, as shown in Fig. 12. These shift can be understandable in the context of the numerous assumptions involved in the derivation of the three SFR tracers. In particular, recent work suggests that for young, low-metallicity galaxies at high redshift the SFRs derived from dust-corrected UV luminosities can be underestimated up to a factor of 2-10 regardless the assumed star formation history. Such discrepancy is due to the solar metallicity implied by the usual β_{UV} - A_{FUV} conversion factor (Castellano et al. 2014). Since our EELGs are characterized by their subsolar metallicities their dust attenuations derived through the Meurer’s formula might be systematically lower than the true ones and, therefore, the derived SFR_{FUV} might be underestimated. This hypothesis is supported in our case by the fact that the SFR derived from the SED (which takes into account the metallicity of the galaxy to choose the best-fit model) is always systematically offset to higher values by ~ 0.2 dex. In agreement with the results by Castellano et al. (2014) if this offset is only due to the dust attenuation correction it would imply that Meurer’s zero-point should be corrected upwards by this quantity for typical EELGs, resulting in a median dust attenuation in the FUV of about ~ 10 -20% higher. Although a rigorous analysis of the discrepancies between different SFR indicators is far from the scope of this paper we caution about using dust attenuation corrections for low-metallicity galaxies under the assumption of models and calibrations which are valid for solar metallicity environments.

3.5. The gas-phase metallicity of EELGs

Given the wide redshift range of the sample, the low S/N of some faint emission lines and the limited wavelength coverage of the VIMOS spectra, the derivation of gas-phase metallicity in our sample of EELGs cannot be addressed using a unique method-

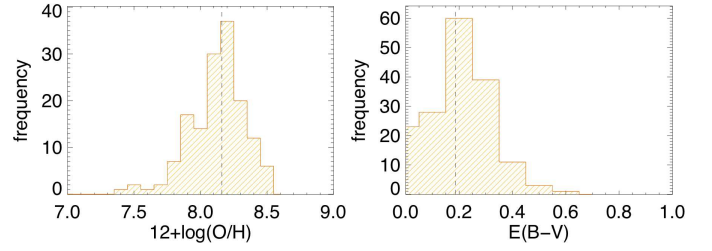


Fig. 13. Distribution of gas-phase metallicity (*left*) and reddening (*right*). Vertical dashed lines indicate median values.

ology. Thus, we follow four different methods to derive metallicities for 149 out of 165 EELGs ($\sim 90\%$ of the sample) with reliable measurements for the required set of lines imposed by these methods, as described below. We show in Fig. 13(*left*) the histogram distribution of the derived gas-phase metallicity for the sample of EELGs. Overall, the metallicities of EELGs span a wide range of $12+\log(\text{O}/\text{H}) = 7.3 - 8.5$, with median value $12+\log(\text{O}/\text{H}) = 8.16$ ($\sim 0.18 Z_{\odot}$). We do not observe any trend with redshift. Median values for both redshift bin and morphological type are presented in Table 2, while the metallicity and associated uncertainty for each galaxy is presented in Table 1⁵, indicating in each case the applied method.

3.5.1. Metallicity derived through the direct method

The direct method (also known as t_e -method) is the most accurate method to derive the oxygen chemical abundance in star-forming galaxies (e.g. Hägele et al. 2008). It is based on the previous determination of the electron temperature of the gas, using the intensity ratio of nebular-to-auroral emission lines (e.g. $[\text{O III}]\lambda\lambda 4959, 5007$ and $[\text{O III}]\lambda 4363$) and the relative intensity of the strongest nebular emission lines to a hydrogen recombination line. Since for the EELGs we do not have a direct estimation of the $[\text{O II}]$ electron temperature, they have been derived using the model-dependent relation between the $[\text{O III}]$ and $[\text{O II}]$ electron temperatures, $t_e [\text{O III}]$ and $t_e [\text{O II}]$, proposed by Pérez-Montero & Díaz (2003), which takes into account the dependence of the latter on the electron density. Then, following the expressions in Pérez-Montero & Contini (2009), O^+ and O^{2+} have been calculated using $t_e [\text{O III}]$ and $t_e [\text{O II}]$ and the relative intensities of the corresponding bright emission lines, namely $[\text{O II}]\lambda 3727$, and $[\text{O III}]\lambda 4363$, plus $[\text{O III}]\lambda\lambda 4959, 5007$, respectively. Finally, O^+ and O^{2+} have been combined to estimate the total abundance of oxygen relative to hydrogen, O/H .

Following the direct method we have derived ionic abundances in 26 purely star-forming EELGs ($\sim 16\%$) uniformly distributed in redshift and with reliable measurements ($S/N > 2$) of all the involved emission lines, including $[\text{O III}]\lambda 4363$. We find direct metallicities spanning a large range of values, $12 + \log(\text{O}/\text{H}) = 7.5$ -8.4.

3.5.2. Metallicity of EELGs without $[\text{O II}]$ measurements: the $t_e [\text{O III}]$ -Z calibration

For EELGs with reliable measurements of the $[\text{O III}]\lambda 4363, 4959, 5007$ lines, but without $[\text{O II}]$ line measurement, i.e. those where $[\text{O II}]$ lines lie out of the VIMOS spectral range, we cannot derive O^+ , so we do not have a direct

⁴ $\mu_{FUV} = \frac{0.5 L_{FUV}}{\pi R_{50}^2}$

⁵ The uncertainties in $12+\log(\text{O}/\text{H})$ only takes into account the propagation of errors from the emission line flux measurements

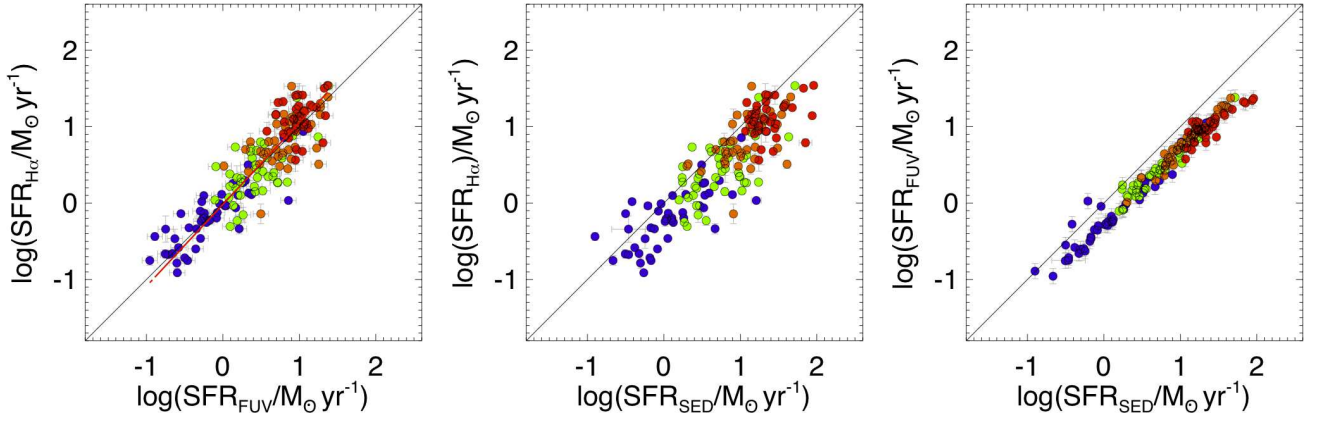


Fig. 12. Rest-frame, attenuation-corrected FUV versus $H\alpha$ star formation rates for the sample of EELGs. The solid line indicate the one-to-one relation, whereas the red dashed line is a linear fit to data.

Table 1. The global properties of EELGs in zCOSMOS-20k

ID	$\alpha(J2000)$ deg	$\delta(J2000)$ deg	z	MT	$M_{B,0}$ mag	$\log L_{FUV,0}$ kpc	r_{50} M_{\odot}	$\log M_{\star}$ $M_{\odot} \text{yr}^{-1}$	$\log \text{SFR}_{H\alpha, H\beta}$ L_{\odot}	$12 + \log(\text{O}/\text{H})$	Method
(1)	(2)	(3)	(4)	(5)	(6)	(7)	(8)	(9)	(10)	(11)	(12)
700882	150.349518	2.275816	0.4638	T	-18.9	10.23	1.02	8.66 ± 0.12	0.45 ± 0.18	$\dots \pm \dots$...
701051	149.856964	2.245983	0.3446	T	-18.06	9.88	1.48	8.32 ± 0.11	0.38 ± 0.03	$\dots \pm \dots$...
701741	150.393982	2.578904	0.5041	...	-18.94	10.15	...	8.41 ± 0.05	0.8 ± 0.11	7.46 ± 0.15	T_e
800984	150.286469	1.623921	0.5955	T	-19.04	10.5	1.54	8.76 ± 0.01	1.03 ± 0.07	7.95 ± 0.07	T_e
801094	150.242004	1.610143	0.5463	...	-19.27	10.29	...	8.77 ± 0.17	-0.14 ± 0.13	8.14 ± 0.1	R23
802275	149.711777	1.616209	0.6349	M	-19.93	10.7	2.22	9.14 ± 0.06	1.13 ± 0.08	8.18 ± 0.06	R23
803226	150.705399	1.716969	0.5696	C	-19.5	10.13	1.72	8.86 ± 0.19	0.41 ± 0.07	7.87 ± 0.1	T_e
803892	150.526794	1.787344	0.4389	C	-18.96	9.96	1.43	8.55 ± 0.23	0.19 ± 0.09	$\dots \pm \dots$...
804130	150.452408	1.632364	0.4293	M	-20.08	9.98	2.21	9.01 ± 0.07	0.33 ± 0.16	8.53 ± 0.12	N2
804791	150.286530	1.633338	0.6025	C	-20.65	11.05	2.02	9.47 ± 0.05	0.51 ± 0.06	8.29 ± 0.16	R23

Columns: (1) zCOSMOS identification number; (2) and (3) Right ascension and declination (J2000); (4) Spectroscopic redshift; (5) Morphological type: (R) Round/Nucleated, (C) Clumpy/Chain, (T) Cometary/Tadpole, (M) Merger/interacting; (6) Rest-frame absolute B-band magnitude; (7) Rest-frame, dust-corrected FUV luminosity; (8) Circularized effective radius; (9) Stellar mass; (10) Star formation rate from $H\alpha$ or $H\beta$ luminosity; (11) Gas-phase metallicity; (12) Method used for metallicity derivation in (10). (The entire version of this table for the full sample of EELGs is available *On-line*).

measurement of the metallicity. In our sample, 19 galaxies ($\sim 12\%$) at $z < 0.48$ fall into this category. For these galaxies, however, we can derive a “semi-direct” metallicity taking advantage of the tight relation between $t_e[\text{O III}]$ and Z expected for high excitation environments – like those present in EELGs – from both observations and models (e.g. Masegosa et al. 1994; López-Sánchez et al. 2012). Thus, we calibrate the relation between $t_e[\text{O III}]$ and Z for EELGs (dubbed hereafter as the $t_e[\text{O III}]-Z$ calibration) using a combination of two independent datasets for which direct measurements of the metallicity are available. We use metallicity measurements derived using the direct method for both giant H II regions and H II galaxies from Pérez-Montero & Contini (2009) and the sample of *green pea* galaxies from Amorín et al. (2010). In order to avoid a strong dependence with the ionizing parameter, the calibration was restricted to those objects with $[\text{O II}]/[\text{O III}]$ ratios in the range covered by the EELG sample (Figure 14, upper left panel).

In Figure 14 (upper right panel) we show the $t_e[\text{O III}]-Z$ calibration, which yields the following expression,

$$12 + \log(\text{O}/\text{H}) = 9.22 (\pm 0.03) - 0.89 (\pm 0.02) t_e[\text{O III}] \quad (1)$$

where $t_e[\text{O III}]$ is the $[\text{O III}]$ electron temperature in units of 10^4 K. Uncertainties in the $t_e[\text{O III}]-Z$ calibration translate into uncer-

tainties of $\lesssim 0.15$ dex (1σ) in metallicity. As a consistency check, we have applied the $t_e[\text{O III}]-Z$ calibration to those EELGs with metallicities derived using the direct method. In Figure 14 we show that the two metallicity estimates based on the electron temperature are in good agreement over the wide range of metallicity covered by our sample, with deviations broadly consistent within the errors. Only a small shift of ~ 0.1 - 0.2 dex is noticed in some cases, especially at lower metallicities. In this range, i.e. $12 + \log(\text{O}/\text{H}) \lesssim 7.7$, the $t_e[\text{O III}]-Z$ calibration has a lower statistical significance and the scatter is large, probably due to an increased sensitivity of $t_e[\text{O III}]$ on the ionization parameter. Therefore, its use on extremely metal-poor galaxies should be considered with care. Moreover, we caution the reader that the calibration presented in Eq. 1 is well suited for determining reliable oxygen abundances only in objects with similar (high) ionization conditions to those shown by the EELGs. Thus, the $t_e[\text{O III}]-Z$ calibration may appear an alternative for other samples of gas-rich galaxies with similar ionization conditions where the limitation in the spectral coverage does not allow a proper determination of the $[\text{O II}]$ flux.

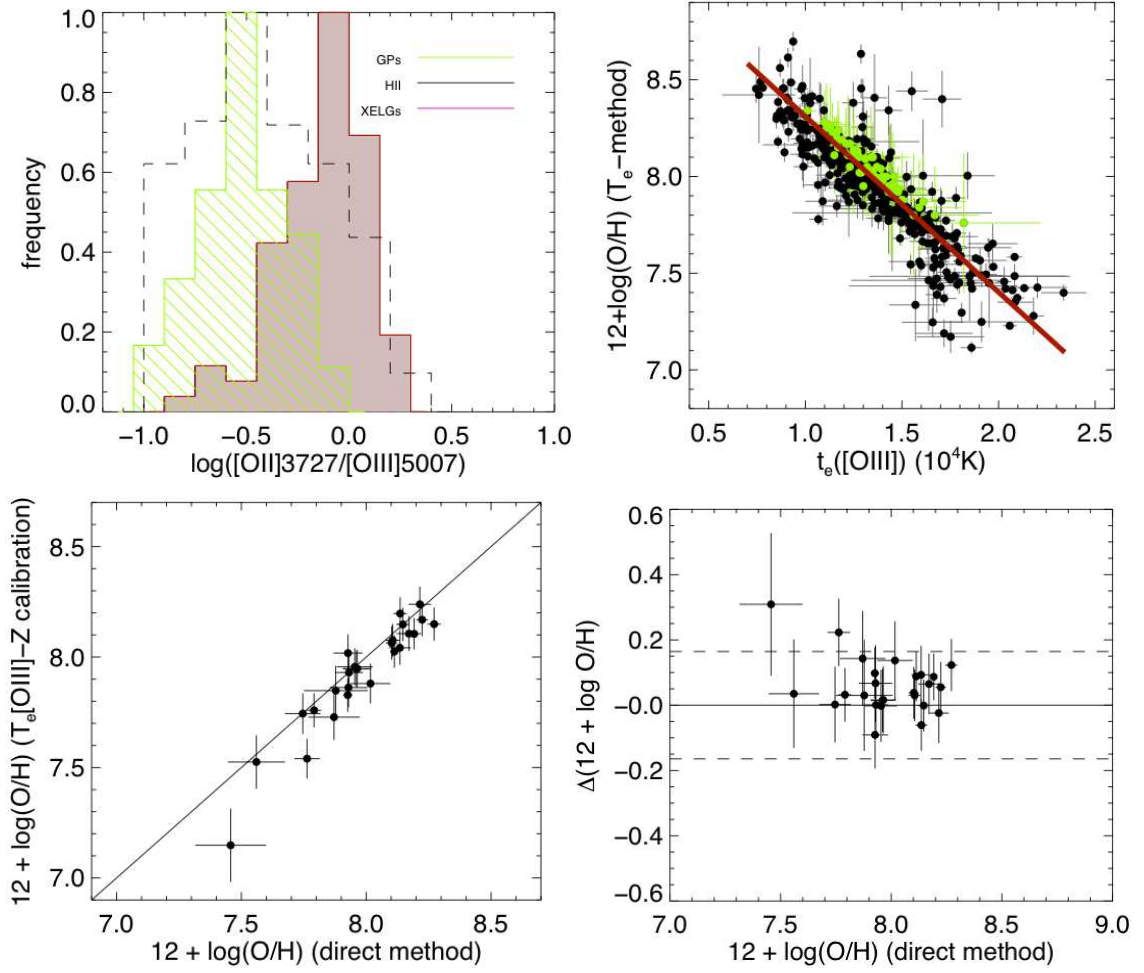


Fig. 14. (*Upper*): The relation between oxygen abundance derived from the direct method and $[\text{O III}]$ electron temperature, as derived from the $[\text{O II}](\lambda 4959 + \lambda 5007)/\lambda 4363$ ratio, is shown in the right panel. The red line indicates the fit according to Eq. 1. Black and green points are the sample of Giant HII regions and nearby HII galaxies from Pérez-Montero & Contini (2009) and the sample of *green peas* from Amorín et al. (2010), respectively. The histogram distributions of the ionization parameter, as measured by the $[\text{O II}]/[\text{O III}]$ ratio, for these samples in comparison with our samples of EELGs are shown in the left panel. (*Bottom*): A comparison between metallicities derived using the direct method and the $t_e[\text{O III}]$ -Z calibration in Eq. 1 and their residuals including 2σ limits are shown in the left and right panels, respectively.

3.5.3. Metallicity from strong-line methods

The two above methods based on the determination of the electron temperature cannot be applied to the whole sample of EELGs either because at certain redshifts the $[\text{O III}]\lambda 4363$ line is not included in the VIMOS spectral range, or because this line is too weak. One alternative for the derivation of the gas-phase metallicity in these galaxies is the use of the so-called “strong-line” methods. These methods are based on the direct calibration of the relative intensity of the strongest collisionally-excited emission-lines with grids of photoionization models or samples of objects with an accurate determination of the oxygen abundance, or both.

There is a large variety of strong-line methods used in the literature, which usually give different results depending on the metallicity range, ionization conditions, and available line ratios (see Kewley & Ellison 2008, for an extensive discussion). In order to derive metallicities consistent with those derived from the t_e -based methods, here we use three different empirical calibrations based on a sample of nearby objects with accurate determinations of $12 + \log(\text{O}/\text{H})$ via the direct (t_e) method. We use the

calibration proposed by Pérez-Montero & Contini (2009) based on the $N2$ parameter, defined as the ratio of $[\text{N II}]\lambda 6584$ to $\text{H}\alpha$ by Storch-Bergmann et al. (1994), and used by Denicoló et al. (2002) as a metallicity proxy. This method is our choice for EELGs at $z \lesssim 0.30$, where $[\text{N II}]$ and $\text{H}\alpha$ are included in the VIMOS spectra but $[\text{O III}]\lambda 4363$ is not. Although this relation does not present any dependence neither on reddening correction nor flux calibration uncertainties, $N2$ depends on the ionization parameter, the equivalent effective temperature and the nitrogen-to-oxygen ratio (Pérez-Montero & Díaz 2005). Taking these effects into account, in EELGs – which show quite homogeneous excitation properties (see Figure 14) – the overall uncertainty is ~ 0.2 dex across their entire metallicity range.

For those EELGs at $z > 0.48$ where the $[\text{O III}]\lambda 4363$ auroral line is too weak to derive $t_e[\text{O III}]$ and $N2$ cannot be applied (i.e., $\text{H}\alpha + [\text{N II}]$ lie out of the spectral range), metallicity is derived using the R_{23} parameter. R_{23} is defined as the ratio between the relative sum of $[\text{O II}]\lambda 3737$ and $[\text{O III}]\lambda\lambda 4959, 5007$ to $\text{H}\beta$ fluxes (Pagel et al. 1979). The main disadvantage of R_{23} is its bi-valued relation with Z . Moreover, R_{23} has a strong depen-

dence on the ionization parameter and effective temperature. To minimize this dependence we use the calibration proposed by Kobulnicky et al. (2003), based on the photoionization models from McGaugh (1991), which includes additional terms as a function of $[\text{O II}]/[\text{O III}]$. Most of the EELGs are located in the elbow of the R_{23} calibration. Therefore, for those galaxies with a difference $\lesssim 0.3$ dex between the metallicity provided by the upper and lower branches we adopt a mean value as the final metallicity. For galaxies where this difference is higher we adopt the upper branch of the $R_{23} - Z$ relation because we interpret the absence of the $[\text{O III}]$ auroral line in high S/N spectra as a possible sign of high ($12 + \log(\text{O}/\text{H}) \gtrsim 8.2$) metallicities. Nonetheless, we note that we do not find EELGs with $12 + \log(\text{O}/\text{H}) > 8.5$.

Finally, it is worth mentioning that important differences may arise from adopting different strong-line methods and/or different calibrations (see e.g. Kewley & Ellison 2008). Here, metallicities derived using the $N2$ method with the calibration by Pérez-Montero & Contini (2009) are consistent with those derived from the direct method. However, the adopted calibration of R_{23} is not based on galaxies with direct metallicities but on grids of photoionization models, which may produce a systematic bias. To overcome these differences, we follow Pérez-Montero et al. (2013) and convert the metallicities derived from R_{23} to those derived from the $N2$ parameter, using the linear relations described in Lamareille et al. (2006b), which are based on models by Charlot & Longhetti (2001). This way, the adopted estimators yield metallicities which are broadly consistent, within the uncertainties, with each other.

4. Discussion

4.1. Discovery of extremely metal-poor EELGs

Extremely metal-poor (XMP) galaxies are the least evolved systems in the Universe and therefore, they provide a unique environment to study the first stages of galaxy evolution and chemical enrichment (Kunth & Östlin 2000). Thus, it is of great interest to examine in detail those EELGs with the lowest metallicities. In our sample of 149 EELGs with reliable metallicities we find only six objects ($\sim 4\%$) with metallicities lower than the typical upper limit for XMPs ($\sim 1/10Z_{\odot}$ ⁶, e.g. Kniazev et al. 2004; Ekta & Chengalur 2010). This is not surprising since XMPs are typically scarce in the local Universe ($\sim 0.01\%$ Morales-Luis et al. 2011) and only a handful of *bona fide* XMPs out to redshift 1-2 have been found to date (e.g. Hu et al. 2009; Ly et al. 2014; Maseda et al. 2014).

The main metallicity properties of the XMPs discovered in zCOSMOS are shown in Table 3, while in Figure 15 we show two examples illustrating their VIMOS spectra at different redshifts. For two EELGs, zCOSMOS 701741 and zCOSMOS 825959, at redshift $z=0.5$ and $z=0.7$, respectively, metallicities have been derived using the direct method. In the lower panel of Figure 15, we show the spectrum of the former, which has the lowest metallicity measured using the $[\text{O III}]\lambda 4363$ auroral line – which is highlighted in the inset figure. For another EELG, zCOSMOS 836108, its metallicity was derived using the $T([\text{O III}]) - Z$ calibration, because its $[\text{O II}]$ line lie out of the VIMOS spectral range. We are cautious about its value because at very low metallicities the $T([\text{O III}]) - Z$ calibration may under-predict the true metallicity (see Figure 14). The remaining three EELGs have $z \lesssim 0.3$. Therefore, their metallicities

were derived using the $N2$ parameter. These three EELGs include zCOSMOS 840952, the lowest metallicity galaxy in our sample ($Z \sim 0.04Z_{\odot}$), well comparable to the most metal-poor H II galaxies known (e.g., IZw 18 and SBS 0335-052 (E&W) Papaderos et al. 2006; Izotov et al. 2009). Its spectrum is shown in the upper panel of Figure 15. In the inset figure we also show the region of $\text{H}\alpha + [\text{N II}]\lambda 6584$. The $[\text{N II}]$ line is extremely weak, with a signal-to-noise ratio of only ~ 2.5 , so its flux measurement may even be an upper limit. Importantly, for these three nearby EELGs where sulfur lines (e.g. $[\text{S II}]\lambda\lambda 6717, 6731$) have been measured, we have derived the nitrogen-to-oxygen ratio (N/O) using the $N2S2$ calibration (Pérez-Montero & Contini 2009). Their very low values, $\log(\text{N}/\text{O}) \lesssim -1.7$, suggest that the low amount of nitrogen is of primary origin, supporting the hypothesis of chemically unevolved galaxies (e.g. Mollá et al. 2006). Deeper, high S/N spectroscopy covering the entire spectral range will provide a definitive confirmation of the extremely low oxygen abundance for these EELGs.

An intriguing aspect of XMPs is that a significant fraction of these chemically unevolved galaxies turn out to have cometary or tadpole morphologies ($>60\%$, Papaderos et al. 2008; Sánchez Almeida et al. 2013; Filho et al. 2013). While tadpole/cometary morphologies are rather common at high redshift ($\sim 6-10\%$ of all galaxies in the Hubble Ultra Deep Field, Straughn et al. 2006; Elmegreen & Elmegreen 2010), their fraction apparently decreases at lower redshifts ($<1\%$ in the local Universe; Elmegreen et al. 2012). As shown in Section 3.1, a significant fraction of zCOSMOS EELGs out to $z \sim 1$ shows cometary/tadpole morphology. These peculiar morphologies, together with their dynamical properties and low-metallicity have been interpreted as signs of disk galaxies in early stages of assembling (Sánchez Almeida et al. 2013). While we find these morphologies in the whole metallicity range, it appears interesting that at least half of the most metal-poor EELGs are tadpoles. In the forming disk scenario proposed for local tadpoles, massive accretion of external metal-poor gas feeds the starburst, leading to large metallicity inhomogeneities or gradients from head to tail (Sánchez Almeida et al. 2014), similarly to those observed at higher redshift (e.g. Cresci et al. 2010; Queyrel et al. 2012; Troncoso et al. 2014).

4.2. Lyman-alpha emission in EELGs

High redshift star-forming galaxies are generally recognized in surveys by their high UV luminosity and/or by their strong $\text{Ly}\alpha$ emission, with equivalent widths $\text{EW}(\text{Ly}\alpha) \gtrsim 20$ (e.g. Shapley et al. 2003; Mallery et al. 2012). Although $\text{Ly}\alpha$ selection may trace systematically different galaxies at different redshifts (Nilsson et al. 2011) and a small fraction of $\text{Ly}\alpha$ emitters (LAEs) may be evolved galaxies (Pentericci et al. 2009), a largest fraction of them typically shows low metallicity, blue colors, small sizes, and low dust attenuation, consistent with being on an early stage of galaxy formation (e.g. Pirzkal et al. 2007; Cassata et al. 2011; Cowie et al. 2011; Finkelstein et al. 2011). A significant fraction of their low redshift ($z \sim 0.3$) analogues are also found to be EELGs (e.g. Cowie et al. 2011).

Though they were not selected by their UV properties, our sample of EELGs are very luminous in the UV continuum, so it is interesting to inspect whether some of these galaxies have been identified as LAEs in the literature. To this end, we cross-correlate our sample with GALEX grism spectroscopy surveys and find that only four zCOSMOS EELGs at $z = 0.25 - 0.38$ have been observed so far (shown in Figure 16). However, it is remarkable that *all* these EELGs, included in the catalogue of

⁶ We have adopted a solar metallicity value of $12 + \log(\text{O}/\text{H}) = 8.69$ (Allende Prieto et al. 2001)

Table 2. Median properties of zCOSMOS EELGs according to their redshift and morphological type.

Redshift bin	N	z	M_B	$c(H\beta)$	r_{50}	β_{UV}	$\log L_{FUV}$	$SFR_{H\alpha, H\beta}$	$\log M_\star$	$12 + \log(O/H)$
Morphological type					kpc		L_\odot	$M_\odot \text{ yr}^{-1}$	M_\odot	
(1)	(2)	(3)	(4)	(5)	(6)	(7)	(8)	(9)	(10)	(11)
1 ($0.11 \leq z \leq 0.30$)	44	0.19	-17.6 (0.9)	0.31 (0.19)	1.6 (1.4)	-1.44 (0.51)	9.6 (0.5)	0.6 (2.6)	8.02 (0.47)	8.10 (0.3)
2 ($0.30 < z \leq 0.50$)	43	0.40	-19.3 (0.7)	0.27 (0.18)	1.3 (1.0)	-1.66 (0.32)	10.2 (0.3)	2.2 (2.4)	8.70 (0.29)	8.07 (0.3)
3 ($0.50 < z \leq 0.70$)	42	0.61	-20.1 (0.7)	0.27 (0.16)	1.5 (0.6)	-1.61 (0.31)	10.6 (0.3)	6.3 (2.1)	9.02 (0.31)	8.16 (0.3)
4 ($0.70 < z \leq 0.93$)	36	0.82	-20.7 (0.4)	0.31 (0.15)	1.0 (0.6)	-1.68 (0.43)	10.8 (0.2)	12.7 (1.7)	9.21 (0.24)	8.21 (0.3)
All-SF	165	0.48(0.23)	-19.5 (1.4)	0.27 (0.17)	1.3 (1.0)	-1.61 (0.41)	10.4 (0.6)	3.9 (3.9)	8.79 (1.07)	8.16 (0.3)
All-SF in groups	46	0.35(0.22)	-18.9 (1.5)	0.31 (0.17)	1.4 (1.1)	-1.55 (0.43)	10.3 (0.6)	2.4 (4.1)	8.72 (1.08)	8.15 (0.3)
Elliptical/Regular	30	0.44 (0.25)	-19.1 (1.4)	0.36 (0.20)	1.0 (0.3)	-1.54 (0.42)	10.2 (0.5)	3.2 (3.6)	8.54 (1.08)	8.13 (0.3)
Clumpy/Irregular	60	0.48 (0.23)	-19.5 (1.5)	0.31 (0.15)	1.5 (0.7)	-1.61 (0.43)	10.3 (0.6)	3.9 (4.3)	8.76 (1.07)	8.14 (0.3)
Tadpole/Cometary	27	0.46 (0.20)	-19.2 (1.4)	0.27 (0.18)	1.5 (0.7)	-1.70 (0.36)	10.3 (0.6)	3.3 (3.7)	8.70 (1.07)	8.08 (0.3)
Merger/Interacting	48	0.55 (0.23)	-20.2 (1.1)	0.27 (0.17)	1.5 (1.5)	-1.55 (0.41)	10.6 (0.5)	6.2 (3.7)	9.05 (1.05)	8.18 (0.3)
NL-AGN	18	0.78 (0.16)	-20.7 (0.8)	0.62 (0.45)	1.15 (0.34)	-1.32 (0.83)	10.9 (0.5)	17.2 (4.4)	9.36 (1.10)	–

Columns: (2) Number of galaxies; (3) median redshift; (4) rest-frame B -band absolute magnitude; (5) reddening; (6) circularized half-light radius (7) UV spectral slope; (8) dust-corrected FUV luminosity; (9) dust-corrected star formation rate; (10) stellar mass; (11) metallicity. In parentheses with include 1σ dispersion for most of these quantities.

Table 3. The properties of very metal-poor EELGs in zCOSMOS-20k.

ID	z	MT	$c(H\beta)$	$EW(H\beta)$	$t_e([O\text{ III}])$	$\log([O\text{ III}]/H\beta)$	$\log([N\text{ II}]/H\alpha)$	$\log(N/O)$	$12 + \log(O/H)$
(1)	(2)	(3)	(4)	(5)	(6)	(7)	(8)	(9)	(10)
701741	0.504	2	0.12	113	2.28 ± 0.11	0.50 ± 0.05	7.46 ± 0.15^b
809215	0.124	2	0.20^a	-1.79 ± 0.18	-1.83 ± 0.15^e	7.65 ± 0.07^d
825959	0.690	3	0.00^a	66	1.87 ± 0.06	0.52 ± 0.06	7.56 ± 0.12^b
836108	0.351	3	0.30	74	1.92 ± 0.04	0.77 ± 0.04	7.47 ± 0.10^c
840051	0.250	1	0.28	84	...	0.61 ± 0.02	-1.75 ± 0.11	-2.00 ± 0.26^e	7.69 ± 0.08^d
840962	0.121	1	0.31^a	-2.18 ± 0.13	-1.75 ± 0.24^e	7.35 ± 0.11^d

Columns: (1) zCOSMOS identification number; (2) Redshift; (3) Morphological type: (1) Regular, (2) Clumpy/irregular, (3) Cometary/Tadpole; (4) Reddening constant from the $H\alpha/H\beta$ ratio, excepting for those with (a) subscript, which are taken from SED fitting; (5) $H\beta$ equivalent width, in Å; (6) $[O\text{ III}]$ electron temperature, in units of 10^4K ; (7) $[O\text{ III}]/5007/H\beta$ ratio; (8) $N2$ parameter; (9) Nitrogen-to-Oxygen ratio; (10) Gas-phase metallicity; Method used to derive metallicity and N/O: (b) =Direct method, (c) = $T([O\text{ III}]) - Z$, (d) = $N2$, (e) = $N2S2$.

low- z GALEX LAEs of Cowie et al. (2010), show prominent $Ly\alpha$ emission lines, with luminosities $\log(L_{Ly\alpha}) = 41.8\text{--}42.4 \text{ erg s}^{-1}$, and high equivalent widths of $EW(Ly\alpha) = 22\text{--}45\text{Å}$.

The observed $Ly\alpha/H\alpha$ ratios of these EELGs are between 0.5–2, well below the Case B recombination value, even after correction by dust extinction. Comparing their $Ly\alpha$ and $H\alpha$ equivalent widths (ranging $EW(H\alpha) = 320\text{--}580\text{Å}$) these galaxies are among those with larger $EW(H\alpha)$ low- z LAEs in the catalogue by Cowie et al. (2010). Their $EW(H\alpha)/EW(Ly\alpha)$ ratios (~ 14) are instead comparable with some high excitation LAEs at higher redshift (e.g. $z \sim 2$ Finkelstein et al. 2011; Nakajima et al. 2013). Compared with model predictions (e.g. Schaerer 2003), these $EW(H\alpha)/EW(Ly\alpha)$ ratios are in good agreement with tracks for instantaneous burst models with young ages ($\sim 10^7\text{yr}$) and low metallicities (see Nakajima et al. 2013, their Figure 10), probably superposed with a more constant (e.g. exponentially declining) underlying star formation history (e.g. Amorín et al. 2012a).

As shown in Figure 16, zCOSMOS EELGs with $Ly\alpha$ emission display different morphologies in HST-ACS imaging. Though they classify as *green pea* galaxies due to their large $EW([O\text{ III}])$ and green colours (see SDSS postage stamps in Fig. 16), these galaxies were not included in the *green pea* sample by Cardamone et al. (2009) because they are much fainter than the SDSS spectroscopic limits. The connection between LAEs, *green peas* and our sample of EELGs is not entirely surprising. Cowie et al. (2011) have shown that a high fraction ($\sim 75\%$) of low- z LAEs have $EW(H\alpha) > 100\text{Å}$, while only $\sim 30\%$ of UV-continuum selected galaxies with $EW(H\alpha) > 100\text{Å}$ are LAEs. Moreover, recent studies have found evidence for high ionization state and low metallicities in LAEs out to $z \gtrsim 2$ (Xia et al. 2012; Nakajima et al. 2013, see also Cassata et al. 2012, for $\text{HeII } \lambda 1640$ detection in LAEs). These two properties are an imprint of *green peas* (Amorín et al. 2012a; Jaskot & Oey 2013) and EELGs in general (see Figure 3). Thus, LAEs could

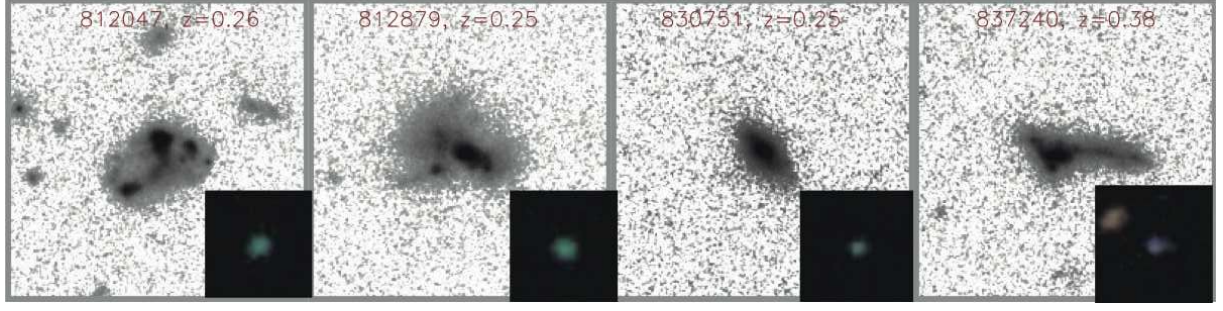


Fig. 16. HST/ACS *I*-band images of EELGs with Ly α line emission. Each panel has 6 arcsec on a side. Labels indicate zCOSMOS ID number and redshift. The insets show the corresponding SDSS-DR9 postage-stamp.

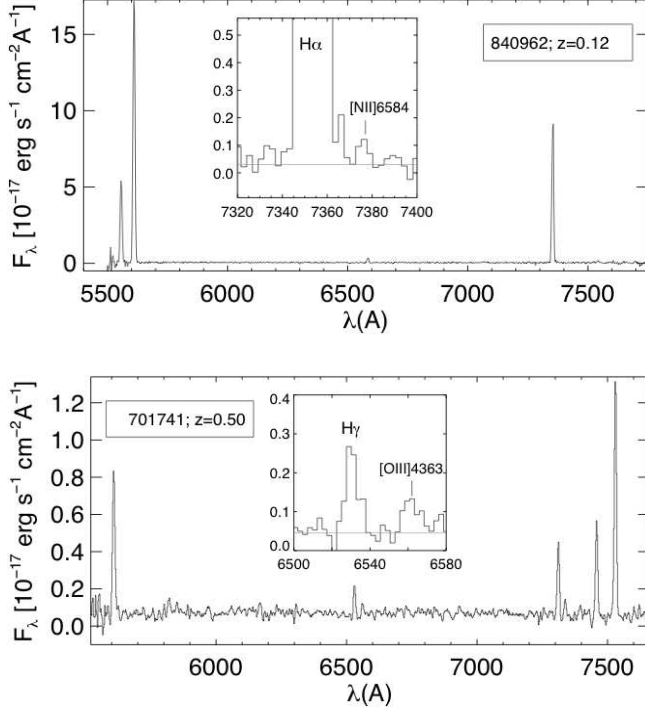


Fig. 15. VIMOS observed spectra of the very metal-poor EELGs 840962 and 701741 at $z = 0.12$ and $z = 0.50$, respectively. The spectra have been smoothed by a 2 pixels filter. The insets show a close-up view of the $H\alpha + [NII]$ and $H\gamma + [OIII]\lambda 4363$ lines.

be ubiquitous among low-mass galaxies selected by their unusually large equivalent widths.

4.3. Morphology and environment of EELGs and their possible connection with other global properties

The characterization of morphology and environment of EELGs and their implications with all their other derived global properties, like metallicity or specific star formation rate, is essential to get insights on galaxy evolution and physical mechanisms driving massive star formation. However, this can be a tricky task, especially in the case of compact and relatively distant galaxies like EELGs. These objects have faint underlying stellar components and usually they look unresolved from the ground, showing us only their high surface brightness components i.e., the starburst, even when observed from the space. Moreover, sensitivity limits and the lack of spectroscopic coverage for faint close neighbours may affect the detection of faint features associated

with ongoing or recent interactions, e.g. stellar or gaseous tails or bridges. In that sense, the combination of deep HST-ACS imaging and spectroscopy from zCOSMOS provides a good starting point for this type of study at intermediate redshift.

4.3.1. Morphology

In Section 3.1, we have presented a first glance of the morphological and environmental properties of EELGs. Using quantitative morphological parameters, we find that EELGs are more compact and irregular in shape than other star-forming galaxies of similar redshift in zCOSMOS. Among EELGs, however, we do not find any clear correlation between e.g. concentration, asymmetry or Gini, and other global properties, i.e. redshift, absolute magnitudes, SFRs, stellar masses, extinction or gas-phase metallicity. In that sense, we do not find significant differences between round/nucleated EELGs and irregular classes, being the latter the conjunction of the other three categories (see Table 2). For example, although EELGs classified as merger/interacting galaxies appear to show enhanced SFRs and dust attenuation, as well as larger stellar masses and metallicities, part of this difference might be attributed to a selection bias, since they tend to have higher redshifts and luminosities in the median. Similarly, round/nucleated EELGs appear more compact and less luminous than irregular classes. However, it is difficult to determine if these differences are intrinsic or a result of a redshift effect. Moreover, a serious limitation in this type of analysis is that EELGs may be affected by surface brightness sensitivity limits, i.e. their underlying stellar components may be more extended at lower surface brightnesses (e.g. Amorín et al. 2009). More detailed work using surface photometry on deeper multi-band images from CANDELS might shed new light to this respect. Overall, our results clearly indicate that EELGs are dominated by non-axisymmetric morphologies, which are likely linked with their early evolutionary stage and starburst nature.

4.3.2. Environment

Regarding the environmental properties we find that EELGs are preferably located in relative isolation, in agreement with previous findings for local star-forming dwarf galaxies (e.g. Vílchez 1995; Lee et al. 2000; Cardamone et al. 2009). Only $\sim 30\%$ of EELGs are grouped, with one or more spectroscopic companions. This result is in good agreement with previous findings for nearby star-forming dwarfs (Telles & Terlevich 1995; Noeske et al. 2001; Pustilnik et al. 2001; Koulouridis et al. 2013). It should be noted, however, that most of these groups show a non-negligible number of additional photometric members, which may constitute in most cases neighbours of lower

luminosity. Due to spectroscopic incompleteness we may miss – in these and in the remaining 70% of the sample – possible faint companions which are often seen projected closely to the EELGs (see, e.g. EELG 812047 in Figure 16), so the above numbers should be considered as lower limits. This limitation could be important to evaluate the influence of the close environment on the star formation activities of EELGs, especially at increasing redshift. Although they are considered isolated systems, observational evidence shows local star-forming dwarfs usually associated with low-surface brightness companions (Brosch et al. 2004; Sánchez-Janssen et al. 2013). If these neighbours are located in the very close environment (<1 Mpc) of the galaxies they may have an influence on the star formation triggering processes and subsequent evolution (Pustilnik et al. 2001). Moreover, interactions or minor mergers with faint, gas-rich companions can lead to inflows of metal-poor gas, shaping the metallicity properties of these galaxies (e.g. Dekel et al. 2009; Sánchez Almeida et al. 2014).

A thorough investigation of the close environment of EELGs in zCOSMOS is needed to compare with similar studies in the local Universe, and to discuss in detail the possible influence of neighbours on the star formation activity and average photometric and spectroscopic properties of non-isolated EELGs, a topic that will be addressed in a future study.

5. Summary and conclusions

In this paper a large sample of 183 galaxies with the largest $[\text{O III}]\lambda 5007$ rest-frame equivalent widths (i.e. $\text{EW}([\text{O III}]) > 100\text{\AA}$) in the zCOSMOS-20k Bright sample has been collected in order to study their main optical and UV properties, including stellar mass, SFR, gas-phase metallicity and dust extinction, as well as morphology and large-scale environment, over the last ~ 8 billion years. We summarize our main findings as follows:

1. Our selection criterion based on $\text{EW}([\text{O III}])$ has yielded 183 EELGs at $0.11 \leq z \leq 0.93$. Thus, EELGs constitute 3.4% of star-forming galaxies in our parent zCOSMOS sample. Using emission-line diagnostic diagrams we divided the sample in 165 purely star-forming galaxies plus 18 NL-AGN candidates ($\sim 10\%$).
2. Using HST-ACS I -band COSMOS images we classify star-forming EELGs in four morphological classes according to the distribution and shape of their high- and low-surface brightness components (i.e. SF knots and host galaxy, respectively). We show that 18% have round/nucleated morphologies, most of them showing nearly unresolved appearance, while the remaining 82% are galaxies with irregular morphologies, visually classified as *clumpy/chain* (37%), *cometary/tadpole* (16%), and *merger/interacting* (29%). Therefore, we conclude that at least $\sim 80\%$ of the EELG sample show non-axisymmetric morphologies. Our visual classification is confirmed using quantitative morphological parameters. We find that the EELGs show smaller half-light radii ($r_{50} \sim 1.3$ kpc in the median) and larger concentration, asymmetry and Gini parameters than other SFGs in zCOSMOS, being most of them classified as *irregular* galaxies in automated classification schemes. We find that both the redshift distribution and main physical properties of EELGs of different morphological classes show no substantial differences.
3. EELGs form the low-end of stellar mass and high-end of sSFR distributions of SFGs in zCOSMOS up to $z \sim 1$.

Stellar masses of EELGs, as derived from multiband SED fitting, lie in the range $7 \lesssim \log(M_*/M_\odot) \lesssim 10$. Star formation rates from both $\text{H}\alpha$ and FUV luminosities after corrections for dust attenuation and extinction are consistent with each other and range $0.1 \lesssim \text{SFR} \lesssim 35 M_\odot \text{ yr}^{-1}$ (Chabrier IMF scale). Both quantities increase similarly with redshift, so this results on a tight range of *specific* SFRs (median $\text{sSFR} = 10^{-8.18} \text{ yr}^{-1}$) and stellar mass doubling times $0.01 \text{ Gyr} < M_*/\text{SFR} < 1 \text{ Gyr}$.

4. EELGs are characterized by their low metallicities, $7.3 \lesssim 12 + \log(\text{O}/\text{H}) \lesssim 8.5$ ($0.05\text{--}0.6 Z_\odot$), as derived using both the direct measurements based on electron temperature (t_e) and strong-line methods calibrated consistently with galaxies with t_e measurements. Therefore, the chemical abundances of EELGs at $0.11 \leq z \leq 0.93$ are very similar to those of nearby HII galaxies and BCDs. We find only six ($\sim 4\%$) extremely metal-poor ($Z < 0.1 Z_\odot$) galaxies in our sample.
5. EELGs are moderately low-dust, very compact UV-luminous galaxies, as evidenced from their typically blue colours ($\beta \sim -1.6$), high FUV luminosities ($L_{\text{FUV}} \sim 10^{10.4} L_\odot$) and high surface brightnesses $\mu_{\text{FUV}} \geq 10^9 L_\odot \text{ kpc}^{-2}$. We find only four EELGs with GALEX-UV spectroscopic observations. All these galaxies are strong $\text{Ly}\alpha$ emitters, with large equivalent widths and luminosities in the ranges $\text{EW}(\text{Ly}\alpha) = 22\text{--}45\text{\AA}$ and $\log(\text{Ly}\alpha) = 41.8\text{--}42.4 \text{ erg s}^{-1}$, respectively.

In conclusion, we have shown that galaxies selected by their extreme strength of their optical emission lines led us to a homogeneous, representative sample of compact, low-mass, low-metallicity, vigorous star-forming systems identifiable with luminous, higher- z versions of nearby HII galaxies and Blue Compact Dwarfs. The extreme properties of some of these rare systems closely resemble those of luminous compact galaxies, such as the *green peas* (Cardamone et al. 2009; Amorín et al. 2010) and other samples of emission line galaxies with very high equivalent widths recently found at similar and higher redshift (e.g. Hoyos et al. 2005; Kakazu et al. 2007; Salzer et al. 2009; Izotov et al. 2011; Atek et al. 2011; van der Wel et al. 2011, 2013; Xia et al. 2012; Shim & Chary 2013; Henry et al. 2013; Ly et al. 2014; Maseda et al. 2014; Amorín et al. 2014b). The EELGs are galaxies caught in a transient and likely early period of their evolution, where they are efficiently building-up a significant fraction of their present-day stellar mass in a young, galaxy-wide starburst. Therefore, they constitute an ideal benchmark for comparative studies with samples of high redshift $\text{Ly}\alpha$ emitters and Lyman-break galaxies of similar mass and high ionization state.

Acknowledgements. We gratefully acknowledge Polychronis Papaderos, Marco Castellano, Veronica Sommariva, Jorge Sánchez Almeida and Casiana Muñoz-Tuñón for a carefully reading of the paper and the helpful comments and suggestions provided. We also thank the referee for his/her helpful comments and suggestions which contributed to improve this manuscript. This work was partially funded by the Spanish MICINN under the Consolidator-Ingenio 2010 Program grant CSD2006-00070: First Science with the GTC⁷, and by projects AYA2007-67965-C03-02 and AYA2010-21887-C04-01 of the Spanish National Plan for Astronomy and Astrophysics, and by the project TIC114 *Galaxias y Cosmología* of the Junta de Andalucía (Spain).

R.A. acknowledge the contribution of the FP7 SPACE project ASTRODEEP (Ref.No: 312725), supported by the European Commission. This work has also been partially supported by the CNRS-INSU and its Programmes Nationaux de Galaxies et de Cosmologie (France). The VLT-VIMOS observations have been carried out on guaranteed time (GTO) allocated by the European Southern Observatory (ESO) to the VIRMOS consortium, under a contractual agreement between the Centre National de la

⁷ <http://www.iac.es/consolider-ingenio-gtc>

Recherche Scientifique of France, heading a consortium of French and Italian institutes, and ESO, to design, manufacture and test the VIMOS instrument. Based on observations obtained with MegaPrime/MegaCam, a joint project of CFHT and CEA/DAPNIA, at the Canada-France-Hawaii Telescope (CFHT) which is operated by the National Research Council (NRC) of Canada, the Institut National des Sciences de l'Univers of the Centre National de la Recherche Scientifique (CNRS) of France and the University of Hawaii. This work is based in part on data products produced at TERAPIX and the Canadian Astronomy Data Centre as part of the Canada-France-Hawaii Telescope Legacy Survey, a collaboration project of NRC and CNRS.

References

- Abazajian, K., Adelman-McCarthy, J. K., Agüeros, M. A., et al. 2003, *AJ*, 126, 2081
- Abraham, R. G., van den Bergh, S., Glazebrook, K., et al. 1996, *ApJS*, 107, 1
- Allende Prieto, C., Lambert, D. L., & Asplund, M. 2001, *ApJ*, 556, L63
- Amorín, R., Alfonso, J., Aguerri, J. A. L., Muñoz-Tuñón, C., & Cairós, L. M. 2009, *A&A*, 501, 75
- Amorín, R. O., Pérez-Montero, E., & Vílchez, J. M. 2010, *ApJ*, 715, L128
- Amorín, R., Pérez-Montero, E., Vílchez, J. M., & Papaderos, P. 2012b, *ApJ*, 749, 185
- Amorín, R., Vílchez, J. M., Hägele, G. F., et al. 2012b, *ApJ*, 754, L22
- Amorín, R., Grazian, A., Castellano, M., et al., 2014a, *ApJ*, submitted
- Amorín, R., Sommariva, V., Castellano, M., et al., 2014b, *A&A*, submitted
- Atek, H., Siana, B., Scarlata, C., et al. 2011, *ApJ*, 743, 121
- Baldwin, J. A., Phillips, M. M., & Terlevich, R. 1981, *PASP*, 93, 5
- Bertoldi, F., Carilli, C., Aravena, M., et al. 2007, *ApJS*, 172, 132
- Bolzonella, M., Kovač, K., Pozzetti, L., et al. 2010, *A&A*, 524, A76
- Brosch, N., Almozino, E., & Heller, A. B. 2004, *MNRAS*, 349, 357
- Bruzual, G. & Charlot, S. 2003, *MNRAS*, 344, 1000
- Bundy, K., Ellis, R. S., Conselice, C. J., et al. 2006, *ApJ*, 651, 120
- Cairós, L. M., Caon, N., Vílchez, J. M., González-Pérez, J. N., & Muñoz-Tuñón, C. 2001, *ApJS*, 136, 393
- Capak, P., Aussel, H., Ajiki, M., et al. 2007, *ApJS*, 172, 99
- Cardamone, C., Schawinski, K., Sarzi, M., et al. 2009, *MNRAS*, 399, 1191
- Cardelli, J. A., Clayton, G. C., & Mathis, J. S. 1989, *ApJ*, 345, 245
- Calzetti, D., Armus, L., Bohlin, R. C., et al. 2000, *ApJ*, 533, 682
- Cassata, P., Le Fèvre, O., Garilli, B., et al. 2011, *A&A*, 525, A143
- Cassata, P., Le Fèvre, O., Charlot, S., et al. 2012, *arXiv:1212.5270*
- Castellano, M., Fontana, A., Grazian, A., et al. 2012, *A&A*, 540, A39
- Castellano, M., et al. 2014, *arXiv:1403.0743*
- Chabrier, G. 2003, *PASP*, 115, 763
- Charlot, S., & Longhetti, M. 2001, *MNRAS*, 323, 887
- Chen, T.-W., Smartt, S. J., Bresolin, F., et al. 2013, *ApJ*, 763, L28
- Christensen, L., Hjorth, J., & Gorosabel, J. 2004, *A&A*, 425, 913
- Cowie, L. L., Barger, A. J., & Hu, E. M. 2010, *ApJ*, 711, 928
- Cowie, L. L., Barger, A. J., & Hu, E. M. 2011, *ApJ*, 738, 136
- Cresci, G., Mannucci, F., Maiolino, R., et al. 2010, *Nature*, 467, 811
- Curtis-Lake, E., McLure, R. J., Dunlop, J. S., et al. 2013, *MNRAS*, 429, 302
- Dekel, A., Birnboim, Y., Engel, G., et al. 2009, *Nature*, 457, 451
- Denicoló, G., Terlevich, R., & Terlevich, E. 2002, *MNRAS*, 330, 69
- Ekta, B., & Chengalur, J. N. 2010, *MNRAS*, 406, 1238
- Elmegreen, B. G., & Elmegreen, D. M. 2010, *ApJ*, 722, 1895
- Elmegreen, D. M., Elmegreen, B. G., Sánchez Almeida, J., et al. 2012, *ApJ*, 750, 95
- Elmegreen, B. G., Elmegreen, D. M., Sánchez Almeida, J., et al. 2013, *ApJ*, 774, 86
- Elvis, M., Civano, F., Vignali, C., et al. 2009, *ApJS*, 184, 158
- Filho, M. E., Winkel, B., Sánchez Almeida, J., et al. 2013, *A&A*, 558, A18
- Finkelstein, S. L., Cohen, S. H., Malhotra, S., & Rhoads, J. E. 2009, *ApJ*, 700, 276
- Finkelstein, S. L., Hill, G. J., Gebhardt, K., et al. 2011, *ApJ*, 729, 140
- Gaia, L., Franke, H., Gawiser, E., et al. 2013, *A&A*, 551, A93
- Guseva, N. G., Papaderos, P., Meyer, H. T., Izotov, Y. I., & Fricke, K. J. 2009, *A&A*, 505, 63
- Guseva, N. G., Izotov, Y. I., Fricke, K. J., & Henkel, C. 2011, *A&A*, 534, A84
- Guzman, R., Gallego, J., Koo, D. C., et al. 1997, *ApJ*, 489, 559
- Hägele, G. F., Díaz, A. I., Terlevich, E., Terlevich, R., Pérez-Montero, E., & Cardaci, M. V. 2008, *MNRAS*, 383, 209
- Hasinger, G., Cappelluti, N., Brunner, H., et al. 2007, *ApJS*, 172, 29
- Hayes, M., Östlin, G., Schaerer, D., et al. 2013, *ApJ*, 765, L27
- Henry, A., Martin, C. L., Finlator, K., & Dressler, A. 2013, *ApJ*, 769, 148
- Hoyos, C., Koo, D. C., Phillips, A. C., Willmer, C. N. A., & Guhathakurta, P. 2005, *ApJ*, 635, L21
- Hu, E. M., Cowie, L. L., Kakazu, Y., & Barger, A. J. 2009, *ApJ*, 698, 2014
- Huertas-Company, M., Rouan, D., Tasca, L., Soucail, G., & Le Fèvre, O. 2008, *A&A*, 478, 971
- Izotov, Y. I., Papaderos, P., Guseva, N. G., Fricke, K. J., & Thuan, T. X. 2006, *A&A*, 454, 137
- Izotov, Y. I., Guseva, N. G., Fricke, K. J., & Papaderos, P. 2009, *A&A*, 503, 61
- Izotov, Y. I., Guseva, N. G., & Thuan, T. X. 2011, *ApJ*, 728, 161
- Jaskot, A. E., & Oey, M. S. 2013, *ApJ*, 766, 91
- Juneau, S., Dickinson, M., Alexander, D. M., & Salim, S. 2011, *ApJ*, 736, 104
- Kakazu, Y., Cowie, L. L., & Hu, E. M. 2007, *ApJ*, 668, 853
- Kauffmann, G., Heckman, T. M., Tremonti, C., et al. 2003, *MNRAS*, 346, 1055
- Kennicutt, R. C., Jr. 1998, *ApJ*, 498, 541
- Kennicutt, R. C., & Evans, N. J. 2012, *ARA&A*, 50, 531
- Kewley, L. J., Dopita, M. A., Sutherland, R. S., Heisler, C. A., & Trevena, J. 2001, *ApJ*, 556, 121
- Kewley, L. J., Brown, W. R., Geller, M. J., Kenyon, S. J., & Kurtz, M. J. 2007, *AJ*, 133, 882
- Kewley, L. J., & Ellison, S. L. 2008, *ApJ*, 681, 1183
- Kniazev, A. Y., Pustilnik, S. A., Grebel, E. K., Lee, H., & Pramskij, A. G. 2004, *ApJS*, 153, 429
- Knobel, C., Lilly, S. J., Iovino, A., et al. 2009, *ApJ*, 697, 1842
- Knobel, C., Lilly, S. J., Iovino, A., et al. 2012, *ApJ*, 753, 121
- Kobulnicky, H. A., Willmer, C. N. A., Phillips, A. C., et al. 2003, *ApJ*, 599, 1006
- Koekemoer, A. M., Aussel, H., Calzetti, D., et al. 2007, *ApJS*, 172, 196
- Koo, D. C., Guzman, R., Faber, S. M., et al. 1995, *ApJ*, 440, L49
- Koulouridis, E., Pionis, M., Chávez, R., et al. 2013, *arXiv:1304.0777*
- Krueger, H., Fritze-v. Alvensleben, U., & Loose, H.-H. 1995, *A&A*, 303, 41
- Kunth, D., Östlin, G. 2000, *A&A Rev.*, 10, 1
- Lamareille, F., Mouhcine, M., Contini, T., Lewis, I., & Maddox, S. 2004, *MNRAS*, 350, 396
- Lamareille, F., Contini, T., Le Borgne, J.-F., et al. 2006a, *A&A*, 448, 893
- Lamareille, F., Contini, T., Brinchmann, J., et al. 2006b, *A&A*, 448, 907
- Lamareille, F. 2007, Ph.D. Thesis
- Lamareille, F., Brinchmann, J., Contini, T., et al. 2009, *A&A*, 495, 53
- Lee, J. C., Salzer, J. J., Law, D. A., & Rosenberg, J. L. 2000, *ApJ*, 536, 606
- Le Fèvre, O., Saisse, M., Mancini, D., et al. 2003, *Proc. SPIE*, 4841, 1670
- Lilly, S. J., Le Fèvre, O., Renzini, A., et al. 2007, *ApJS*, 172, 70
- Lilly, S. J., Le Brun, V., Maier, C., et al. 2009, *ApJS*, 184, 218
- López-Sánchez, Á. R., Dopita, M. A., Kewley, L. J., et al. 2012, *MNRAS*, 426, 2630
- Lunnan, R., Chornock, R., Berger, E., et al. 2013, *ApJ*, 771, 97
- Ly, C., Malkan, M. A., Nagao, T., et al. 2014, *ApJ*, 780, 122
- Mallery, R. P., Mobasher, B., Capak, P., et al. 2012, *ApJ*, 760, 128
- Maraston, C. 2005, *MNRAS*, 362, 799
- Marocco, J., Hache, E., & Lamareille, F. 2011, *A&A*, 531, A71
- Martin, D. C., Fanson, J., Schiminovich, D., et al. 2005, *ApJ*, 619, L1
- Maseda, M. V., van der Wel, A., da Cunha, E., et al. 2013, *ApJ*, 778, L22
- Maseda, M. V., et al., 2014, *ApJ*, submitted
- Masegosa, J., Moles, M., & Campos-Aguilar, A. 1994, *ApJ*, 420, 576
- Masters, D., McCarthy, P., Siana, B., et al. 2014, *arXiv:1402.0510*
- McCracken, H. J., Capak, P., Salvato, M., et al. 2010, *ApJ*, 708, 202
- McGaugh, S. S. 1991, *ApJ*, 380, 140
- Meurer, G. R., Heckman, T. M., & Calzetti, D. 1999, *ApJ*, 521, 64
- Mollá, M., Vílchez, J. M., Gavilán, M., & Díaz, A. I. 2006, *MNRAS*, 372, 1069
- Monreal-Ibero, A., Walsh, J. R., Westmoquette, M. S., & Vílchez, J. M. 2013, *A&A*, 553, A57
- Morales-Luis, A. B., Sánchez Almeida, J., Aguerri, J. A. L., & Muñoz-Tuñón, C. 2011, *ApJ*, 743, 77
- Nakajima, K., Ouchi, M., Shimasaku, K., et al. 2013, *ApJ*, 769, 3
- Nilsson, K. K., Östlin, G., Møller, P., et al. 2011, *A&A*, 529, A9
- Noeske, K. G., Iglesias-Páramo, J., Vílchez, J. M., Papaderos, P., & Fricke, K. J. 2001, *A&A*, 371, 806
- Overzier, R. A., Heckman, T. M., Kauffmann, G., et al. 2008, *ApJ*, 677, 37
- Pagel, B. E. J., Edmunds, M. G., Blackwell, D. E., Chun, M. S., & Smith, G. 1979, *MNRAS*, 189, 95
- Papaderos, P., Izotov, Y. I., Fricke, K. J., Thuan, T. X., & Guseva, N. G. 1998, *A&A*, 338, 43
- Papaderos, P., Guseva, N. G., Izotov, Y. I., et al. 2006, *A&A*, 457, 45
- Papaderos, P., Guseva, N. G., Izotov, Y. I., & Fricke, K. J. 2008, *A&A*, 491, 113
- Pentericci, L., Grazian, A., Fontana, A., et al. 2009, *A&A*, 494, 553
- Pérez-Montero, E. & Díaz, A. I. 2003, *MNRAS*, 346, 105
- Pérez-Montero, E. & Contini, T. 2009, *MNRAS*, 398, 949
- Pérez-Montero, E. & Díaz, A. I. 2005, *MNRAS*, 361, 1063
- Pérez-Montero, E., Contini, T., Lamareille, F., et al. 2013, *A&A*, 549, A25
- Pettini, M., Shapley, A. E., Steidel, C. C., et al. 2001, *ApJ*, 554, 981
- Phillips, A. C., Guzman, R., Gallego, J., et al. 1997, *ApJ*, 489, 543
- Pirzkal, N., Malhotra, S., Rhoads, J. E., & Xu, C. 2007, *ApJ*, 667, 49
- Pustilnik, S. A., Kniazev, A. Y., Lipovetsky, V. A., & Ugryumov, A. V. 2001, *A&A*, 373, 24

- Queyrel, J., Contini, T., Kissler-Patig, M., et al. 2012, A&A, 539, A93
- Rosa-González, D., Schmitt, H. R., Terlevich, E., & Terlevich, R. 2007, ApJ, 654, 226
- Salzer, J. J., Williams, A. L., & Gronwall, C. 2009, ApJ, 695, L67
- Sánchez Almeida, J., Muñoz-Tuñón, C., Elmegreen, D. M., Elmegreen, B. G., & Méndez-Abreu, J. 2013, ApJ, 767, 74
- Sánchez Almeida, J., Morales-Luis, A. B., Muñoz-Tuñón, C., et al. 2014, ApJ, 783, 45
- Sánchez-Janssen, R., Amorín, R., García-Vargas, M., et al. 2013, A&A, 554, A20
- Sanders, D. B., Salvato, M., Aussel, H., et al. 2007, ApJS, 172, 86
- Sargent, W. L. W., & Searle, L. 1970, ApJ, 162, L155
- Savaglio, S., Glazebrook, K., & Le Borgne, D. 2009, ApJ, 691, 182
- Searle, L., & Sargent, W. L. W. 1972, ApJ, 173, 25
- Scoville, N., Aussel, H., Brusa, M., et al. 2007, ApJS, 172, 1
- Schaerer, D. 2003, A&A, 397, 527
- Schaerer, D., & de Barros, S. 2009, A&A, 502, 423
- Shapley, A. E., Steidel, C. C., Pettini, M., & Adelberger, K. L. 2003, ApJ, 588, 65
- Schiminovich, D., Wyder, T. K., Martin, D. C., et al. 2007, ApJS, 173, 315
- Schinnerer, E., Smolčić, V., Carilli, C. L., et al. 2007, ApJS, 172, 46
- Shim, H., & Chary, R.-R. 2013, ApJ, 765, 26
- Stark, D. P., Schenker, M. A., Ellis, R., et al. 2013, ApJ, 763, 129
- Storchi-Bergmann, T., Calzetti, D., & Kinney, A. L. 1994, ApJ, 429, 572
- Storey, P. J., & Hummer, D. G. 1995, MNRAS, 272, 41
- Straughn, A. N., Cohen, S. H., Ryan, R. E., et al. 2006, ApJ, 639, 724
- Taniguchi, Y., Scoville, N., Murayama, T., et al. 2007, ApJS, 172, 9
- Tasca, L. A. M., Kneib, J.-P., Iovino, A., et al. 2009, A&A, 503, 379
- Telles, E., & Terlevich, R. 1995, MNRAS, 275, 1
- Terlevich, R., Melnick, J., Masegosa, J., Moles, M., & Copetti, M. V. F. 1991, A&AS, 91, 285
- Thuan, T. X., & Martin, G. E. 1981, ApJ, 247, 823
- Tremonti, C. A., Heckman, T. M., Kauffmann, G., et al. 2004, ApJ, 613, 898
- Troncoso, P., Maiolino, R., Sommariva, V., et al. 2014, A&A, 563, A58
- Trump, J. R., Weiner, B. J., Scarlata, C., et al. 2011, ApJ, 743, 144
- van der Wel, A., Straughn, A. N., Rix, H.-W., et al. 2011, ApJ, 742, 111
- van der Wel, A., van de Ven, G., Maseda, M., et al. 2013, ApJ, 777, L17
- Veilleux, S., & Osterbrock, D. E. 1987, ApJS, 63, 295
- Vílchez, J. M. 1995, AJ, 110, 1090
- Xia, L., Malhotra, S., Rhoads, J., et al. 2012, AJ, 144, 28
- Yan, R., Ho, L. C., Newman, J. A., et al. 2011, ApJ, 728, 38
- Zamojski, M. A., Schiminovich, D., Rich, R. M., et al. 2007, ApJS, 172, 468